DOE/JPL-956053-84/05
JPL NO. 9950-914

Progress Report

to the

U.S. Department of Energy Jet Propulsion Laboratory

Flat-Plate Solar Array Project

January 1984

Contract No. 956053

Surface Property Modification of Silicon

by

Steven Danyluk

This report summarizes the work of J. C. Clark, D. S. Lim and S. W. Lee, graduate students in the Department of Civil Engineering, Mechanics and Metallurgy at the University of Illinois at Chicago.

This work was performed for the Jet Propulsion Laboratory, California Institute of Technology, and was sponsored by the United States Department of Energy through an agreement with the National Aeronautics and Space Administration.

TABLE OF CONTENTS

SURFACE PROPERTLY MODIFICATION OF SILICON

by

Steven Danyluk

Department of Civil Engineering, Mechanics and Metallurgy
University of Illinois at Chicago
Chicago, Illinois 60680

ABSTRACT

This progress report summarizes the work carried out at the University of Illinois at Chicago in the period of September 1, 1981 - December 31, 1983 for the Jet Propulsion Laboratory Flat-Plate Solar Array Project under Contract No. 956053. The main emphasis of this work has been to determine the wear rate of silicon in fluid environments and the parameters that influence wear. Three tests were carried out on single crystal Czochralski silicon wafers: circular and linear multiple-scratch tests in fluids by a pyramidal diamond simulated fixed-particle abrasion; microhardness and three-point bend tests were used to determine the hardness and fracture toughness of abraded silicon and the extent of damage induced by abrasion.

The wear rate of (100) and (111) n and p-type single crystal Cz silicon abraded by a pyramidal diamond in ethanol, methanol, acetone and de-ionized water was determined by measuring the cross-sectional areas of grooves of the circular and linear multiple-scratch tests. The wear rate depends on the loads on the diamond and is highest for ethanol and lowest for de-ionized water. The surface morphology of the grooves showed lateral and median cracks as well as a plastically deformed region. The hardness and fracture toughness are critical parameters that influence the wear rate. Microhardness tests were conducted to determine the hardness as influenced by fluids. Median cracks and the damage zone surrounding the indentations were also related to the fluid properties. A measure of the crack lengths emanating from the

indents showed that at loads representative of abrasion, a dislocation mechanism should be used to account for the damage zone.

Three-point bend tests were performed on single crystal Cz silicon that contained a single linear groove formed in the presence of a fluid. The fracture strength was ralated to the groove radius which in turn was related to the fluid used to form the groove and, the mirror radius of the fracture surface. The measurement was used to determine the fracture toughness of the abraded silicon and the damage zone resulting from the abrasion. The fracture toughness for silicon abraded in ethanol, acetone and air is 0.72, 0.81 and 1.78 $MN/m^{3/2}$ respectively.

The mechanism by which the fluids influence wear is still not completely understood. Fluids apparently influence crack initiation and propagation and, dislocation formation and mobility.

ACKNOWLEDGEMENTS

This work is supported by the U. S. Department of Energy/Jet Propulsion Laboratory Solar Array Project under Contract No. 956053 with S. Danyluk as the principal investigator. This support is gratefully acknowledged. Thanks are due to Drs. K. Koliwad, A. Morrison and J. Liu of the Jet Propulsion Laboratory (JPL) for encouragement and support of this work. S. Hyland and C. P. Chen provided input on the technical direction and T. Daud and M. Leipold provided encouragement throughout the study. We thank them for this interest. The silicon wafers used in this study were provided by S. Hyland of JPL and J. Farber of Monsanto. Special thanks go to M. Naegele and C. Scott for technical assistance.

Summary

The objective of this experimental program was to study the wear of silicon and to determine the influence of water-based fluids and n-alcohols-commonly used in abrasive cutting-on wear. Fixed particle abrasion in fluids was simulated by an inverted pin-on-disk apparatus in which a single crystal pyramidal diamond was dead-weighted and positional above a rotating single crystal Cz silicon wafer so that a circular multi-scratch groove is made in the presence of a fluid. The cross-sectional area at the (110) cleavage planes of the abraded groove was examined in a scanning electron microscope. For given experimental conditions, the size of the groove area and the morphology of the abraded surface may be used to evaluate the influence of fluids on wear. The abraded surfaces contain a damage zone, consisting of lateral and median cracks and, a plastically deformed region. Both participate in the wear process and their influence is reflected in the hardness and fracture toughness parameters in wear models. As expected, the wear rate depends on the load on the diamond - the wear rate increases as the load increases - but fluids also have a dramatic effect on wear. The wear rate in ethanol is three times that in de-ionized water if all other experimental variables are constant.

A microhardness test (Vickers) was conducted on single crystal Cz silicon used in the multi-scratch abrasion tests. Many fluids could be used in this relatively simple test and we have determined the hardness of (100) and (111) n- and p-type silicon in a variety if n-alcohols and in deionized water containing dissolved inorganic salts NaCl,NaBr,NaI,$CaCl_2$ and $FeCl_3$. Hardness values in the n-alcohols were used in wear models that describe the abrasion of brittle materials due to scratching indenters. The inorganic salts dissolved in de-ionized water were used to determine the influence of anion radius and cation valence on hardness. Cracks that emanate from the apexes of

the pyramidal indents were also measured and used to compare to models of fracture of brittle materials. The Vickers hardness may vary by 30% depending on the n-alcohol, being smallest for ethanol and largest for deionized water. The median crack length depends on the ion size and charge of the salt dissolved in the de-ionized water. At loads <0.14N, crack lengths are much smaller than predicted by currently accepted theories of fracture of brittle materials.

A three-point bend test (ASTM D 790) of a single crystal Cz silicon rectangular plate containing a multi-scratch groove formed in either ethanol, acetone or air was used to deduce the fracture toughness. The test localized the fracture on the (110) cleavage plane and, the groove area and mirror radius were measured in the SEM. The fracture toughnesses for ethanol, acetone and air are: 0.72, 0.81 and 1.78 $MN/m^{3/2}$ respectively. These values are the result of the type of damage sustained in the linear multi-scratch test.

The results presented in this report support the current models of abrasive wear of brittle materials. In addition, these results underscore the importance of hardness and fracture toughness as parameters in predicting wear. The results may also be used to verify that plasticity does indeed take place beneath indenters at room temperature.

Page intentionally left blank

pg 6

Page intentionally left blank

1. INTRODUCTION

Abrasive cutting and polishing are used extensively in the processing of glasses, ceramics and semiconductors. Both are similar deformation processes by which a substrate is plastically deformed and cracked by the rubbing or sliding of a hard particle, usually in the presence of a fluid, across the surface. The abrasive particle sizes and forces determine the width and depth of a scratch and ultimately the efficiency of cutting and, the smoothness and damage zone beneath the polished surface.

Glass used for optical windows and poly- and single crystalline ceramics used as substrates for semiconductor switching circuits are routinely cut and polished [1]. In the semiconductor industry, large-scale integrated circuits that use silicon as a substrate, are produced from doped and oriented single crystal boules that are sliced into wafers which are subsequently lapped and polished by diamond and Al_2O_3 abrasives [2]. Wafering and polishing are labor intensive and, when improperly carried out, can result in optical windows that have poor reflectivity or semiconductors devices that have high electron-hole recombination centers due mainly to the damaged surface region. In addition, the surface cracks may lead to unexpected brittle failures [3].

Abrasive cutting and polishing are particularly important process steps for the photovoltaic industry where, in order to compete as cost effective energy sources, solar cells must be inexpensive to manufacture, have a high efficiency and a long predictable service life. Solar cells utilizing silicon are fabricated on thin flat silicon sheet that is produced by cutting wafers from a single or polycrystalline boule or by growing thin sheet directly from the melt. In wafering, SiC or diamond particles are embedded in circular or blade saws that slide across the silicon surface. Microchips of silicon are formed and carried away by a slurry composed of carrier fluid and wear debris. These chips represent lost material which may be reclaimed but this represents

additional cost in solar cell production. A damage zone is introduced into the cut surface and must be removed or the efficiency of the cell will be reduced. Furthermore, wafering may introduce microcracks which may act as failure initiation sites and decrease to overall life of the cell. The silicon materials costs and the manufacture of silicon into sheet represents 30% of the cost of the solar cell. Therefore, even a small improvement in the efficiency of wafering or polishing can represent a large cost saving in solar cell processing.

We report here the results of a research effort on the microscopic mechanisms of abrasion of silicon: the rate of cutting, damage on the cut surface and the influence of forces and fluids on these processes. The objectives of this study are to simulate in a laboratory experiment currently used silicon wafering techniques and determine the wear rate of silicon in candidate fluids. Single crystal (100) and (111) n- and p-type Cz silicon wafers were abraded by a 136° pyramidal diamond at a velocity of 3 cm/s. The wear rates are compared to models of abrasion of non-metals. The Vickers hardness in fluids and three-point bend tests of a silicon wafer containing a linear scratch were carried out from which the hardness and fracture toughness were obtained.

The results are presented in three sections:

1. The wear rate of silicon in common laboratory solvents ethanol, acetone, methanol was determined and compared with the wear rate in de-ionized water. Two models of abrasion were compared to the experimental data.
2. Indentation of silicon in n-alcohols and de-ionized water containing inorganic salts was carried out. The hardness, size of the damage zone and median crack length as a function of the fluid properties was measured.
3. The fracture strength of silicon after abrasion in fluids was determined.

These results are used to determine the fracture toughness and the depth of damage beneath the abrasion grooves.

2. BACKGROUND

2.1 Description of Wafering

Silicon is sliced into sheet or wafers by one of three methods: (a) inner diameter wafering, (b) multi-balde wafering using a slurry and (c) multi-wire wafering using a fixed abrasive and/or a slurry. A schematic of these three processes is shown in Fig. 1. These methods rely on abrasive wear for cutting by the rubbing of diamond or SiC impregnated wires, blades and wheels. The abrasive may be bonded or loose in which case water or an oil-based fluid is used as a carrier.

The abrasives slide across the surface and form a groove as the silicon is removed in the form of microchips. The groove width, called a kerf, depends on the string or blade thickness and the damage mechanism of the silicon. If the abrasive particles are loose, then they may move relative to one another and possibly rotate while sliding across the wearing surface. As wear proceeds, a damage zone which consists of cracks and a plastically deformed region is generated and propagated into the surrounding surfaces beyond the immediate contact area.

The deformation patterns of the scratched surfaces include chevron marks and cracks [4]. Subsequent passes cause crack branching, the cracks propagate further and the material is removed in the form of microchips. Chevron marks can guide the cracks out of the sliding direction and into preferred cleavage planes. The crack length may be large since cleavage stresses are low and the surface region that is affected will extend into the silicon surface. This damaged region must be removed since it can reduce efficiency of electronic circuits and be the cause of fracture. Figure 2 shows a schematic of the

string wafering technique. The fixed abrasives (diamond or SiC) rub against the silicon and generate a damage zone on both surfaces of the wafer. The wear rate, damage zone depth and kerf width depend on a number of experimental variables: force on the string, size, density and geometry of the abrasive, fluid and speed of the string. A minimum in kerf is desireable since the kerf volume represents lost material which will increase the cost of solar cell processing. A fast abrasion rate is required because this reduces processing time and, a minimum in surface damage is required since the removed of this region will lengthen any subsequent processing. The mechanical or chemical polishing of the wafer after cutting represents further loss of silicon. In addition, the damage zone must be removed since this zone is a high defect region which will reduce the efficiency of the cell.

The mechanism of abrasion is one in which the initial scratch generates median and lateral cracks and possibly a damage zone. Subsequent scratches propagate the damage zone into the wafer. Models based on this mechanism have been used to describe the abrasion and wear of brittle materials. These models take into account the cracks and plastic zone generated beneath scratches made by hard abrasive particles but, in general, have no provision to consider the influence of environmental conditions on material removal rates. In addition, the models have been applied principally to the abrasive wear of amorphous materials and where loads on the abrasive particles are high. These models do not account for the variation of hardness or fracture toughness with environmental conditions.

2.2 Stresses in Static and Moving Contacting Solids

The abrasion of silicon in wafering is analogous to the sliding of an indenter on a solid surface. Assuming that the indenter geometry remains unchanged in this process, the stresses that are generated may be sufficient

to cause either plastic deformation or fracture. A starting point for an abrasion model should be a determination of the stresses imposed by the contact of two solid bodies. The studies of stresses that result from the contact of solids data back to Hertz [5] who developed the relationships between contact stresses, fracture conditions and geometries of two contacting solids. Hertz found that the static contact between a spherical indenter of radius 'r' and a flate specimen results in a maximum tensile stress $_m$ within the area contact 'a' such that

$$\sigma_m = (1 - 2\nu)\ P/\pi a^2$$

where

$$a^3 = \frac{4}{3}\,\xi\, Pr/E$$

and

$$\xi = \frac{9}{16}\,[(1-\nu^2) + (1-\nu'^2)(E/E')]$$

where P is the normal load on the indenter, E and E' are the Young's moduli of the specimen and indenter, respectively, and ν and ν' are the corresponding values of the Poisson ratios.

When this stress reaches a value of P_c, a ring crack initiates close to the circle of contact. It had also been found empirically [6] that P_c is proportional to r. These early analyses have been used to describe an indentation test where a hard solid of a given geometry is indented into a flat specimen and the indentation geometry is a refelction of the mechanical properties of the specimen [7]. The stress distribution beneath standard geometries or indenters--Vickers, Knoop and spherical ball--can be obtained from the Hertz analysis. Figure 3 shows the results of a calculation of the stresses generated in an indentation test and the contours of the principle normal stresses in the plane containing the contact axis as obtained by Frank

and Lawn [8]. This figure shows the distribution of the three principal stresses σ_{11}, σ_{22} and σ_{33} beneath the indenter. The stresses were calculated in terms of the mean pressure $P/\pi a^2$ with $\nu = 0.3$. The stress distribution will change with the geometry of the indenter.

This analysis has been extended by a number of workers most notably Lawn [9] who showed that for an amorphous material such as glass, the length of the ring crack is directly related to the load as

$$P/c^{3/2} = \text{constant}$$

For diamond cubic materials, Lawn [10] found that the condition for crack growth will depend on the crystal symmetry.

The stresses outside the contact area vary [11] as

$$\sigma_r = \sigma_m \, a^2/r'^2$$

where σ_m is the maximum Hertz stress defined above and a and r' are the contact area and radial distance away from the point of contact, respectively. In addition to the cone cracks which relieve the stresses, residual stresses are also developed beneath indenters [12].

The residual stresses in metals result from generation of dislocations and the formation of dislocation tangles whose strain fields extend beyond the contact zone. In the case of ceramics, semiconductors and glasses, microcracks and twins are generated and plastic flow is suppressed.

The stress imposed as a result of moving spherical indenters have also been carried out [13,14]. When an indenter slides over a surface, frictional stresses increase the tensile stress at the rear of the contact. For a spherical indenter, the radial stress is modified to [14]

$$\sigma_r = \frac{1-2\nu}{2\pi r^2} \quad P(1+A\mu) \quad .$$

where r is the radius of the indenter, P is the normal force, μ is the coefficient of friction and

$$A = \frac{3\ (4+\nu)}{8(1-2\nu)}$$

Taking $\mu = 0.1$ as a typical value for diamond in air and $\nu = 0.2$, the factor $(1 + A\mu)$ equals 1.8, i.e., the effect of sliding approximately doubles the stress caused by static contact. In vacumm, $\mu \cong 1$ so that the stresses are multiplied by 10.

Moving pointed indenters have been analyzed [15] and the results show that the tensile and shear stresses extend radially and tangentially away from the contact area. Stresses outside the contact area will generate and propagate dislocations or twins which will influence the material removal rate and the extent of the damage zone beneath the indenter. The environmental influence on this damage zone has not been studied to date but there are indications that this influence on the damage zone is significant.

2.3 Wear Rate of Non-metals due to Sliding Indenters

The volume removal rates of non-metals have been calculated from consideration of two models: one by Rabinowicz and co-workers [16] and the other by Evans [17]. The former derived a relationship for abrasive wear by a rigid conical asperity sliding through a distance S while under a load P. This model is shown in Figure 4. If the slider has an apex angle θ and the substrate has hardness H, the indenter generates a contact area (with radius r) related to the load P such that

$$\pi r^2 = P/H$$

The projected area of the indenter below the surface is

$$A_{projected} = rx = r^2 \tan \theta$$

If the indenter is moved laterally by an amount S the volume of material swept out will be

$$V = A_{projected} S$$

Substitution for $A_{projected}$ and r^2 we get the volume of material removed as

$$V = \frac{PS\tan\theta}{\pi H}$$

The Evans model assumes that the sliding indenter imposes stresses that generate lateral cracks and a plastic zone. A schematic of the sliding geometry and the residual stress along a plane through the intersection of the plastic zone with the penetration axis is shown in Figure 5. The spatial variation of the stress along a plane through the location of the maximum stress is approximated as

$$\sigma = \sigma_{peak} (1-r/2a) \qquad r < 2a$$

$$\sigma = 0 \qquad r > 2a$$

The volume removal rate V is then

$$\dot{V} = \frac{0.58}{(\pi\beta)^{7/6}} \cdot \frac{P^{7/6}}{K_{I_c}{}^{2/3} H^{1/2}} \cdot \dot{\ell}$$

where K_{I_c} and H are the fracture toughness and hardness respectively. The sliding distance is ℓ, P is the normal force and $\beta = 2/\pi$ for a Vicker's

pyramid diamond.

The wear rates may be determined from these models if the hardness and fracture toughness are known. These models will be compared in a later section to experimentally determine wear rates.

2.4 Environmental Influences on the Surface Mechanical Properties of Non-metals.

Fluids have been found to influence the surface hardness of non-metals and this effect, usually referred to as the Rehbinder-Westwood effect, is attributed to the pinning of dislocation cores by adsorbates. Fluid adsorption, which is related to the surface potential, can account for a variation of the fracture properties as well as hardness. In both cases, the wear rate can be influenced.

Comprehensive surveys of the present state of knowledge of the effects of fluids on the surface mechanical properties of non-metals have recently been published [18] and will not be reviewed here. We will summarize only those parts of previous studies that deal with semiconductors and the influence of light, fluid and voltage on the surface mechanical properties of silicon.

The surface mechanical properties of silicon can be modified either by light (photo-mechanical effect), fluids (chemo-mechanical effect) or electrostatic potential. A modification of the surface hardness of silicon by photon irradiation was first reported by Kuczynski and Hochman [19]. A softened layer (70% softening) of one to two microns as determined from Knoop indentations when 2.0-4.0 μm wavelength light was shone on the surface. This softening was related to light intensity and surface preparation. The effect was interpretated in terms of energy states of dislocations and space charge layers in the silicon. The infrared and ultraviolet light was thought to alter the energy of the dislocations in the space charge region and thereby

affect the plastic properties.

Ablova [20] investigated the microhardness of silicon as a function of surface preparation, humidity and impurity content. A softening of the surface was observed and depended on the impurity concentration and ambient H_2O. The affect was described in terms of space charge layers and interaction with charged dislocations formed in the deformation process. The influence of the ambient environment on the surface softening was not explained.

Westbrook and Gilman [21] found that a softening (up to 60%) occurred in silicon (2-3 μm deep) when indentations were carried out in the presence of a small potential (0.05-10 v) between the indenter and the silicon surface. The effect disappeared at elevated temperatures and was not sensitive to whether n- or p-type silicon was used. A model or mechanism was not proposed.

The effects of fluids on the hardness of silicon were examined by Yost and Williams [22] who reported a minimum in hardness for n- and p-type silicon with NaCl and $Na_4P_2O_7$ concentration in water with a maximum in the negative zeta potential. The zeta potentials were obtained after crushing the silicon on which hardness tests were performed. Their results indicated that the hardness is related to the surface charge and the charge carrier concentration at the surface. The surface charges were thought to interact with charged kinks at dislocations.

Recently Cuthrell [23] reported that when silicon was drilled in the presence of CCl_4 and H_2O the surface appearance changed from ductile ploughing to brittle fracture for these two fluids respectively. The affect was speculated to be due to hydrogen embrittlement.

Chen and Knapp [24] reported no time-dependent fracture of silicon when stressed in water, salt water, dilute solutions of NH_4OH and HNO_3 and acetone. These results were interpreted to mean that static loads do not influence cracking of silicon.

Kuan, Shih, Van Vechten and Westdorp [25] examined the effect of lubricants on the structure of the surface damage induced in silicon by a 3600 rpm rotating abrasive wheel. Water, methyl silane, kleenzol B and dielectric oil were used as slurries and the damage (dislocations and surface cracks) within the surface region was investigated by optical and transmission electron microscopy. The density of dislocation etch pits beneath the abraded surfaces was lower for kleenzol B and methyl silane as compared with dielectric oil. A positive potential on the silicon increased the depth to which dislocation pits were found and decreased it for a negative potential. These effects were interpreted as lubricant dampening the out-of-plane blade vibration which reduces the surface damage.

Table I shows a summary of the effects of fluids on the surface hardness of silicon. As can be seen, a softening of up to 80% has been reported, depending on the external variables and type of experiment used in the study. These workers have measured the surface mechanical deformation by microhardness indentation - a test which generates dislocations and microcracks. The depth of this damage zone has not been determined except in one case [25].

The depth in this damage zone can however significantly influence wear especially in a multi-scratch test where the sliding asperity generates a plastic zone and cracks that propagate with each traverse.

3. EXPERIMENTAL PROGRAM

The experimental objective of this program was to determine the wear rate of silicon abraded in fluids. A multi-scratch diamond abrasion test and, microhardness and three-point bend tests were performed in well-characterized fluids and the tests were designed to obtain the wear rate, depth of damage and fracture properties of single crystal Cz silicon. Wafering by fixed diamond impregnated strings at ~60 cm/s [26] or circular blades at 3600 rpm is carried out in fluids that are typically water-based. The strings that contain micron-sized diamonds that contain cleavage facets are subjected to loads of 0.8 N although loads as high as 2.8 N have been used [26]. Since the loads are distributed over the length of the string, the load on each diamond will generally be lower than 0.8 N. Our abrasion experiments were designed to simulate diamond impregnated string wafering where the loads ranged from 0.14 to 0.49 N and the scratching speed was ~5 cm/s. At loads lower than 0.14 N the time to obtain a measurable wear was excessive and at velocities higher than 5 cm/s the mechanical stability of the diamond could not be controlled. Pyramidal diamonds at a fixed rake angle were used so that the stress state in the silicon could be described analytically. The damage zone beneath multiple-scratch grooves was determined by fracturing (100) and (111) n- and p-type Cz silicon in a three-point bend test which localized the fracture surface. The fracture stress was measured and the mirror radius determined by SEM. The fracture toughness was determined from these data. Indentation in fluids was accomplished in order to deduce the hardness. These data were used to determine the abrasion rate from two models.

3.1 Wear Rates Measured by the Circular Multi-Scratch Test

The experimental apparatus was designed to simulate cutting by the sliding of a hard particle across the silicon surface. A schematic of the

experiment is shown in Fig. 6 [27]. This apparatus is similar to the pin-on-disk design used in abrasive wear testing with the exception that the abrasive particle is a single crystal pyramid diamond with an apex angle of 136°. The silicon rotates at a fixed speed past a dead-weighted diamond which is positioned to continually traverse one path such that a multi-scratch circular groove is formed. The depth of the groove depends on the time of abrasion, the force on the diamond and speed of rotation. The silicon wafer is positioned on a platten, the surface covered with a fluid, and the dead-weighted diamond is fixed above the rotating platten. One fluid per silicon wafer is used. A series of grooves are formed, each groove corresponding to a given apex and rake angle of the diamond, fluid, dead load force P and time of abrasion.

Figure 7 shows a schematic of the cross-sectional view of the pyramidal diamond sliding on the surface of a solid. The leading edge of the diamond generates compressive stresses while the trailing edge produces tensile stresses which generate microcracks and a plastic zone in the silicon. Cracks that initiate at the abraded surfaces or in the tensile zone and propagate toward the free surface are called lateral cracks. Those that propagate perpendicular to the surface are called median cracks.

Prior to abrasion, the surfaces were cleaned in the following way. The silicon is dipped in a 10 v/o hydrofluoric acid (HF) bath for 30 s, rinsed in de-ionized water and dryed, then immediately immersed in the fluid for testing. The silicon wafers had previously been lapped, polished and etched according to semiconductor industry standards.

After a set of grooves is formed, the wafer is removed, the back scribbed and the wafer sectioned into quarters. The fracture surfaces are $\{110\}$ and the groove cross-sectional areas as well as the abraded surfaces are examined in the scanning electron microscope (SEM). Figure 8 shows the geometry of the

sectioning and the locations of the examined areas. Figure 9 is an SEM micrograph of (100) n-type silicon abraded by a pyramidal diamond for 5, 10 and 20 min. and shows the relative positions of the circular grooves and the morphology of the abraded surfaces. Higher magnification SEM micrographs of the surfaces abraded in de-ionized water, ethanol, acetone and 5 w/o NaCl in de-ionized water are shown in Fig. 10. The experimental conditions in this case were: normal force (P) was 0.098 N and the abrading time was 1.8×10^3 s, all other variables being held constant. As can be seen the groove surface morphology is noticeably different when the fluid is changed, similar to the results previously reported [27]. Conchoidal fracture of the side walls occurs near the top surface and is a result of lateral cracks propagating in the plane of the silicon surface. Micrographs showing this fracture are shown in Fig. 11. Here is shown a terraced structure with the terrace steps containing subsidiary cracks. Also is shown an unusually large debris particle whose surface replicates the terrace steps. In general, the debris particles were of a spectrum of sizes whose surfaces were composed of cleavage facets.

Typical cross-sectional fracture surfaces of (100) and (111) p-type surfaces are shown in Fig. 12. These micrographs show grooves abraded for 1.8×10^3 s in ethanol, acetone and de-ionized water with a pyramidal diamond dead-weighted with P = 0.49 N. These four surfaces show lateral cracks which propagate toward the surface and median cracks directly below the apex of the groove. As can be seen, the morphology of these microcracks vary with fluid. The cracks are shallow and short for ethanol and not as numerous and long for de-ionized water. These samples were heat treated for 1 hr at 1000°C and etched in for S in order to reveal dislocation pits. During heat treatment the strain fields of the dislocations that comprise the plastic zone exert forces on the leading dislocations which propagate away from the damage zone

under the action of these residual stresses. The SEM micrographs in Figure 13 show dislocation etch pits that had propagated away from the damage zone. The pit symmetry verifies the (100) character of the silicon surface.

The cross-sectional area of the groove at the (100) cleavage surfaces were recorded at the four positions on the sectioned wafer and the average area versus abrading time for the fluids methanol, ethanol, acetone and deionized water was recorded. The results are shown in Figs. 14, 15, 16 and 17. These figures show the cross-sectional area ($x10^{-9}$ m^2) versus abrasion time (s) for (100) p-type silicon abraded by a 136° pyramidal diamond. As expected, the cross-sectional area increases linearly with abrasion time and normal force P on the diamond. The rate of abrasion varies from fluid-to-fluid and at $P = 0.49$ N the rate is highest for ethanol and lowest for deionized water. When the geometry of the diamond was changed, for example, because of diamond fracture or wear or, when conical or elliptical diamonds were used, the wear rate was reduced as expected since the load is then distributed over a larger area so that the stresses are lowered.

We have compared these experimental results with the models of Rabinowicz [16] and Evans [17]. In the Rabinowicz model the expression relating the volume V of material removed to the hardness H and the geometry of the cone was given previously as

$$V = \frac{PS \tan \theta}{H}$$

where θ is the slope angle of the cone measured from the plane of the surface. This equation also applies for the circular multiple-scratch case if it is assumed that for each circumferential distance S_i a volume V_i is removed. The total volume is found by summing S_i and V_i. Substituting $S = t(\omega r)$, $V = 2\pi rA$, $\omega = 0.56$ rev s^{-1}, $\theta = 22°$, where t is the abrading

time, r is the radius of the abrading groove and A is the projected area of the penetrating cone in the vertical plane, the area can be expressed as

$$A = \frac{\tan \theta \omega \, P}{2 \pi^2 H} \cdot t$$

The slope of the experimentally determined Area vs. t curve can be compared to the above equation.

In the Evans model the abraded volume removal rate V is related to the fracture toughness K_{I_c} and hardness H by the equation

$$V = \frac{0.58}{(\pi\beta)^{7/6}} \cdot \frac{P^{7/6}}{K_{I_c}{}^{2/3} H^{1/2}} \cdot \ell$$

where ℓ is the sliding distance, P the normal force and $\beta = 2/$ for a Vicker's pyramid diamond. This equation for the single-scratch test is identical to the multiple-scratch case when the V_i are summed over the total path length $\ell = 2 r\pi$.

The cross-sectional area can be obtained from the above equation by substituting $V = 2\pi rA/t$ so that

$$A = \frac{0.58}{(\pi\beta)^{7/6}} \cdot \frac{P^{7/6} \cdot \omega}{K_{I_c}{}^{2/3} H^{1/2}} \cdot t$$

where $\omega = 0.56$ rev s^{-1}. Both models rely on a knowledge of the hardness H and, in addition the Evans model requires the fracture toughness K_{I_c}. The hardness has been shown to be dependent on fluid environment as discussed in section 2.3 of this report and the fracture toughness K_{I_c} will also be influenced by fluid environment through the surface tension γ. The hardness values of various surfaces of silicon in the appropriate fluid were obtained

using a Vicker's hardness tester with a range of loads from 0.15-9.8 N on the indenting diamond for 15 s (Section 3.2 describes these results). The hardness values for (100) n-type silicon indented with 0.15 N were 1.8, 1.5, 1.65 and 1.3 x 10^{10} Nm^{-2} for de-ionized water, methanol, acetone and ethanol, respectively. These values of H are used to determine dA/dt from Eqs. (1) and (3). The fracture toughness was determined from a measure of the fracture mirror diameter (Section 3.3 describes these results) of (100) Cz silicon scratched under ethanol, acetone, water and air. Fracture toughness of surfaces containing a linear scratch was K_{I_c} = 0.73 $MN/m^{3/2}$ for ethanol and is lower than reported by Chen and Leipold [28]. Since the hardness varied with the fluid and load on the indenting diamond, the slopes of the cross-sectional areas versus time derived by Eqs. (1) and (3) will change accordingly.

Figures 18 and 19 show the calculated slopes of the cross-sectional areas versus time when values of hardness and fracture toughness of ethanol are substituted in equations and plotted versus load. The loads were 0.15 N and 0.49 N. These figures show that for the ethanol parameters, the Evans' slope is steeper than the Rabinowicz slope. This differences in slope for the two models will remain for all fluids so that the experimental measurement could be used to distinguish between the two models. Also plotted on these figures is the abrasion rate for ethanol. As can be seen, at a normal force of 0.15 N the data fall generally below the Evans slope and much higher than the Rabinowicz slope. As the load is increased to 0.49 N, the experimentally determined wear rates are larger than the calculated rates for the Evans model indicating that some additional parameter is influencing the abrasion mechanism. The slopes of the A vs. t curves for the four fluids also varied with load as shown in Fig. 20. The slope of this curve can also be used to distinguish between the Rabinowicz and Evans models since it should be

proportional to P and $P^{7/6}$ As can be seen, as the load increases the wear rates deviate from the prediction of either model. These differences in wear rate can be attributed directly to the variation of the hardness and fracture toughness as the fluids are varied and in order to emphasize this we have listed in Table II the wear rates (at P = 0.49 N) for the two models as compared with the experimental results. The wear rates in ethanol, methanol and acetone as compared with water indicate that the hardness is a dominant parameter in the wear rate and it is influenced by the fluid. As the load is decreased the effect of fluid on the hardness is increased. There is no provision, however, in either model to account for the variation of hardness or fracture toughness with fluid.

3.1.1 *Mechanism of Silicon Abrasion*

The results of our experiments confirm the following mechanism of abrasion:

(a) The initial scratch generates a damage zone consisting of a plastically deformed region revealed by our annealing experiments and lateral and radial cracks as shown in the SEM micrographs. The size of this zone which extends beyond the diamond contact area, depends on the load on the diamond and fluid.

(b) Each subsequent pass propagates the damage zone as wear proceeds. The hardness of this region and crack propagation by cleavage is influenced by the fluid.

Evidently when the forces on the diamond are not sufficient to cause fracture and propagate cracks, fluids may affect wear by influencing the generation and propagation of dislocations. Figures 21 and 22 show schematics of the side and front views of the diamond sliding on silicon and the propagation of the damage zone as wear proceeds. The nature and size of this damage zone is

discussed in the following section.

3.2 DEPTH OF DAMAGE STUDIES

The influence of fluids on the depth of damage due to abrasive wear has been studied by two techniques: measurement of the crack lengths and damage zone surrounding microhardness indentations formed in the presence of fluids and, a measure of the fracture mirror radius of abraded specimens fractured in a three-point bend test. The former provided the hardness and the latter the fracture toughness both of which are required as input parameters in the wear models. The microhardness experiments were conducted with two classes of fluids: de-ionized water and common laboratory solvents and, deionized water containing dissolved inorganic cations and anions since the adsorption characteristics for these ions is known. The three-point bend tests to date have only been conducted in de-ionized water and ethanol.

3.2.1 Microhardness Tests

Microhardness tests of (111) p-type and (100) n-type silicon were conducted in specific fluids. Prior to testing, wafers of (111) p-type and (100) n-type silicon were cleaned by immersing in a 10% hydrofluoric acid wash for 30 secs, rinsing in de-ionized water and then air drying. Microhardness testing was carried out using the Shimadzu Microhardness Tester with a 136^{o} pyramid diamond. A 10 mm by 9 mm region of the sample's polished surface was examined for testing with the 40x objective. With a micropipet, fluid was applied to form a large drop between the indenter and testing surface. Testing in acetone and absolute ethyl alcohol required repeated application of fluid. Indentations were made successively at 1.0 mm intervals to produce a rectangular grid of twenty five indentations.

The microhardness was then calcualted from the expression

$$H = \frac{1854.4\ P}{d^2} \quad (kg/mm^2)$$

where d is the length of the diagonal in micrometers and P is the load on the diamond which varied from 0.15 to 9.8 N (15 to 1000 gf).

3.2.2 Microhardness in Laboratory Solvents

The fluids used were reagent grade: methanol, absolute ethanol, glycerol, toluene, acetone and de-ionized water with dielectric constants of: 36, 24, 42.5, 2.4, 21 and 79, respectively. Care was taken to use previously unopened bottles of these fluids. The microhardness was determined by averaging the 25 indentations.

The results of these experiments are shown in Figs. 23 and 24 where the microhardness, H, is plotted as a function of ε, the dielectric constant of the fluid. As can be seen, for a given fluid, the hardness decreases as the load is increased, and the hardness decreases as the dielectric constant approaches 28, being 30% lower for ethanol as compared with toluene or de-ionized water when p=0.15N. There appears only a slight dependence of the microhardness on the n- and p-type character and surface orientation of the silicon wafers.

3.2.3 Microhardness in De-ionized Water Containing Inorganic Ions

Microhardness tests of (111) p-type and (100) n-type Cz silicon were conducted when the surfaces were immersed in de-ionized water containing varying concentrations NaCl, NaBr, NaI, $CaCl_2$ and $FeCl_3$. These salts dissociate in water and contribute charged cations and anions which adsorb on the surface. The anion radius and cation valence could be varied with the above fluids and the adsorption properties of these ions may be described by adsorption isotherms. The indentations were carried out as a function of load

on the diamond. The surfaces were prepared as mentioned in the previous section. The indented region contained median cracks emanating from the apexes of the indents and a damage zone whose area of influence was well beyond the indented region. Two examples of the types of surface morphologies that result after indentation is shown in Figures 25 and 26 which show optical micrographs of indents in (100) and (111) p-type surfaces indented in 10^{-3} M/l NaI after 2 hour soaking. The indenting loads were varied from 9.8N to 1.96N. These figures show that the cracks exhibit the four-fold symmetry of the (100) surface while cracks are generated in the preferred [112] type directions for the (111) surfaces.

The indentation diagonals were used to determine the hardness as a function of fluid concentration and load on the indenting diamond and it was found that the immersion time of the silicon in the fluid influenced the hardness. Figure 27 shows this variation for the microhardness of (100) p-type silicon indented with 0.49 N for 15 s in a 10 ppm $CaCl_2$ solution. As can be seen, the microhardness decreases with soaking time and stabilizes at a uniform value of 11.8 x 10^9 Pa after a period of two hours. A 2 hour soaking time was therefore chosen as the standard time after which the indentations were made. The microhardness for (100) n- and p-type silicon indented with a diamond loaded to 0.49 N versus electrolyte concentration (NaCl, $CaCl_2$ and $FeCl_3$) is shown in Figs. 28 and 29. These figures show that hardness decreases (~20%) with concentration and reaches a minimum at ~100ppm. There appears only a minor influence of the valence on the variation of microhardness. The hardness was also found to vary with load and Fig. 30 shows this variation of hardness for (111) p-type silicon indented in 10^{-3} M/l NaI. Hardness increases when the load is decreased contrary to what is observed in metals. There appears a transition at ~1N at which point there is a dramatic increase in hardness.

The indentations were Sirtl etched for 25s and further examined in the SEM. The plastic damage in the vicinity of the indentation etched more rapidly that the surrounding undamaged regions and a rumpled surface surrounding the indentation was revealed. Two examples, a (100) n-type indentation formed in 1.7 x 10^{-3} M/Ω NaCl with P=0.49 N and, a (111) p-type indentation with P=0.98N formed in 100 ppm NaCl, NaBr and NaI are shown in Figs. 31 and 32. The damage zone extends to the ends of the cracks for the (100) n-type silicon and, the damage has progressed only to 1/2 the crack lengths for the (111) p-type silicon. This damaged region can be identified with dislocations that have been produced in this room-temperature deformation test.

The diameter of this damage zone D, and the lengths of the median cracks c, have been determined to date for indentation formed in NaI, NaBr and NaCl in (111) p-type silicon. Both parameters varied with salt concentration and Figs. 33 and 34 show examples of this variation. As the load on the indenting diamond was increased, c and D increased proportionally. Figures 35 and 36 show this increase in D and c vs. load for (111) p-type silicon indented in 10^{-3} M/l NaI. Fig. 35 shows that there is a linear relationship between the crack lengths and load. These data have been compared to the model proposed by Lawn and there appears a significant deviation of our data with the this model. This deviation especially a low loads can be attributed to the plastic zone formed during indentation. As dislocations and twins are formed, crack lengths are expected to decrease.

3.2.4 Fracture Strength and Fracture Toughness of Single Crystal Cz Silicon Abraded in Ethanol, Acetone and De-Ionized Water

Single crystal (100) p-type silicon wafers were scribbed into 77.7 x 19.3 x 0.61 mm rectangular plates. The samples were dipped in a 10% HF bath for 30

s, rinsed in de-ionized water, dried and immersed in either ethanol, acetone or de-ionized water prior to scratching. A linear multi-scratch groove was then made along the ⟨110⟩ long-axis of the sample by a 136° pyramidal diamond with a tip radius of 10μm. The diamond was dead-weighted in the scratching test with a 0.54 N load and the depth of the groove formed depended on the number of scratches. The fracture strength was measured in air at room temperature in a three-point bending method (ASTM D 790). Fig. 37 shows a schematic of the test geometry. The dimension of the support span was 2.54 cm and the roller radius was 0.318 cm. The tests were carried out in an Instron Model TTD Universal Testing Machine using a 20 lb full-scale load cell. The strain rate was 0.005 in/min. The fracture surface containing the groove and damage-zone was examined by scanning electron microscopy.

Figure 38 shows an SEM micrograph of a (110) cleavage fracture surface which contains the groove cross-section and damage zone for this location along the groove length. Fracture surfaces typically contain a mirror, mist and hackle region and the schematic inset shows the relative positions of these three regions as observed in the above micrograph and which are expected on the fracture surfaces of beam-type sample geometries [29]. The areas of the grooves and the mirror distance from the center of the groove to the initiation site of the hackle region are measured and these are related to the fracture strength. The area of the abraded groove at the (110) cleavage surfaces was measured in the SEM and this area increased as the number of scratches increased. The wear rate as measured by the slopes of the abraded area vs. the number was largest for ethanol and smallest for de-ionized water. These results confirmed the abrasion rates obtained from the circular multi-scratch tests. The fracture strength versus (groove area)$^{1/2}$ is shown in Fig. 39. Each data point represents the fracture strength at this particular position on the groove. Since a variation in the crack geometries and size of

the damage zone beneath each groove is expected the strength varies with each groove and for each fluid. The data show that as the groove area increases the fracture strength stabilizes to a constant value which varies for the three cases shown in the figure. This result implies that the damage zone, which consists of microcracks and a plastic zone beneath the groove, dominates the fracture strength since for a given groove area the fracture strength should not vary since the groove area represents a small percentage of the total area of fracture surface. The strength in air was highest while that in ethanol was lowest. These results emphasize the connection between the damage zone and abrasion rate since the strength is inversely proportional to the abrasion rate. The length, density and orientation of the microcracks and the size of the damage zone are therefore expected to play an important role in abrasive wear. The bending strength versus (mirror distance)$^{-1/2}$ is plotted in Fig. 40. As can be seen, the slopes for each fluid are linear and the slopes are different for the three fluids. The slope of the above curves are related to the mirror constant 'A' and fracture toughness 'K_{I_c}' and all the data were expected to fall on a single straight line. The fracture toughness 'K_{I_c}' can be obtained from the mirror constant 'A' from [30].

$$A = \sigma_F \, d_m^{1/2} = \frac{1}{2} \cdot Y \cdot K_{I_c} \frac{1}{(c/d_m)^{1/2}}$$

where Y = 1.12 is a geometrical factor for a penny shaped flow and, c/d_m is the mirror to flaw size ratio = 13:1 for our case. Therefore,

$$A = 2.86 \, K_{I_c}$$

Table III shows the K_{I_c} values ($MN/m^{3/2}$) calculated from the above equation. These values are 0.72, 0.81 and 1.78 $MN/m^{3/2}$ for ethanol, acetone and air, respectively.

A fracture toughness value of 1.78 $MN/m^{3/2}$ in air is double the reported value of 0.95 $MN/m^{3/2}$ for (100) single crystal silicon when fractured under bending at room temperature [28]. A large value of fracture toughness has been reported previously [31] and it has been attributed to the adsorption of energy by microcracks especially in materials where plastic deformation by dislocation motion is difficult. An increase of a factor of two in the mirror constant was also explained in this way. These studies are supported by results of Cook, et al. [32] who showed that machined surfaces are more resistant to degradation than polished surfaces and Clarke [33] who showed that the damage zone increase the fracture toughness.

DISCUSSION

The abrasion of ceramics, glasses and semiconductors has been the subject of many studies over the years. These studies have been conducted by scratching and indenting Al_2O_3 and MgO, soda-lime glass and silicon, germanium and cadmium telluride. It has been found that abrasion and indentation results in microcracks and a plastic deformation zone. For example, when ceramics are indented with Knoop or Vicker's indenters, a median and lateral crack system along with a plastic zone is developed [34,35,36,37].

When the indenting loads range from 5-400 N, the length of the cracks and their dependence on the indenter geometry and load are predicted by a Hertzian analysis [37]. Threshold loads, however, are not well predicted [38]. An analysis of the subsurface radial crack length shows that the length is proportional to $P^{2/3}$ [39] for amorphous materials such as soda-lime glass. The plastic zone beneath indenters has also been characterized. Dislocation etch pits have been observed directly in LiF [40] and a damage zone radius indirectly measured beneath indented regions in SiC [41]. These regions in this case extend to ~50 μm beneath the indentation. Fracture and plastic

patches have also been observed in germanium when indented at room temperature by loads from 1-100 g [42]. Scratching experiments have also been carried out in soda-lime glass, magnesium alumino-silicate glass-ceramics [32] and in the glass-water system [43]. Fatigue analyses [44] show that the fatigue life depends on the scratching parameters and that the contact residual stresses play a vital role in determining the crack velocity exponent. In addition, annealing of the scratches results in the strength increasing which implies that dislocation tangles must be present beneath the scratches.

Indentation and scratching experiments have also been carried out in silicon. Dislocations have been directly observed by TEM after indentation of (111) surfaces [45,46,47]. In an X-ray study [48], a compressive zone was found beneath scratches formed at room temperature and the distortion zone, interpreted as dislocation tangles was found to exceed the tract width, by several orders of magnitude. Annealing of scratches made at room temperature [49,50] also showed that dislocations propagated away from the indented region. Their motion was thermally activated but could not be annealed out completely. Indentations at high temperature showed that dislocation emanaged from the indented region and form rosettes the length of which could be measured [51] and nucleation and glide of dislocations occurs at the onset of the ductile-to-brittle transition [52] which is also dependent on strain.

These studies confirm that both a crack and deformation region exists beneath indenters and scratches, the extent and severity of which will influence fracture properties. The above studies have been performed at relatively high loads where fracture mechanics can be used to describe the fracture and damage zone size.

Our results show that when the loads on sliding abrasives is low, the mechanism of damage influenced by the properties of the fluids and the surface orientation of the silicon. As the loads are increased, cracks are formed and

propagate on repeated scratching. The indentation tests suggest that dislocations are generated at room temperature beneath indenters.

The role of the fluids in cracking and dislocation generation is still not clear. Apparently, adsorption of the fluids takes place and the interaction between the fluid molecules and dislocations which intersect the surface modifies the dislocation mobilities and/or the efficiency of dislocation sources. As the loads on the indenting or scratching diamonds are increased the fracture strength is attained before yield and, cleavage fracture then occurs. Adsorbates may influence the surface tension and thereby the fracture properties of silicon.

REFERENCES

1. The Science of Ceramic Machining and Surface Finishing II, NBS Special Publication 562, U.S. Department of Commerce (1979) 1.

2. Silicon Device Processing, NBS Special Publication 337, U.S. Department of Commerce, Nov. 1970.

3. C. P. Chen, Interoffice Memorandum, Jet Propulsion Laboratories, Fracture Mechanics Analysis of Spectolab Solar Module, Block II, Failed at Natural Bridges National Momentum, Utah.

4. Misra, A. and Finnie, I., J. Mater, Sci., 14 (1979) 2567.

5. Hertz, H. in Hertz's Miscellaneous papers, Chaps. 5 and 6, London, MacMillan (19).

6. Auerback, F., Ann. Phys. Chem. 43, 61 (1891).

7. The Science of Hardness Testing and Its Research Applications, ed. J. H. Westbrook and H. Conrad, American Society for Metals, Metals Park, OH (1973).

8. Frank, F. C. and Lawn, B. R., Proc. Royal Soc. 299A: 291 (1977).

9. Lawn, B. R., J. Mater. Sci. 16 (1981) 1769.

10. Lawn, B. R., J. Appl. Phys. 39 (10) 1968, 4828.

11. Finnie, I. and Vaidyanathan, S., Fracture Mech. of Ceramics, Vol. 1, Concepts, Flaws and Fractography, eds. R. C. Brandt, D. P. H. Hasselman and F. F. Lange, Plenum, NY (1974).

12. Petrovic, J. J., J. Amer. Cer. Soc. 66(4) (1983) 277.

13. Hamilton, G. M. and Goodman, L. E., J. Appl. Mech., June (1966) 371.

14. Conway, J. C. and Kirchner, H. P., J. Mater. Sci. 15, 2879 (1980).

15. Chiang, S. S. and Evans, A. G., J. Amer. Cer. Soc. 66 (1) (1983) 4.

16. Rabinowicz, E., Dunn, L. A. and Russell, P. G., Wear 4, 345 (1961). Rabinowicz, E., Friction and Wear of Materials, Wiley, NY (1965).

17. Evans, A. G. in The Science of Ceramic Machining and Surface Finishing II, NBS Special Publication 562, U.S. Department of Commerce (1979), p. 1.

18. Proc. NATO Advanced Study Institute on Surface Effects in Crystal Plasticity, Hohegesis, Sept. 5-14, 1975, Noordhoff, Leiden (1977) 629.

19. Kuczynski, G. C. and Hochman, R. F., Phys. Rev. 108 (4), 946 (1957).

20. Ablova, M. S., Soviet Physics - Solid State 6, 2520 (1965).

21. Westbrook, J. H. and Gilman, J. J., J. Appl. Phys. 33(7) 2360 (1962).

22. Yost, G. H. and Williams, W. S., J. Amer. Cer. Soc. 61(3) 139 (1978).

23. Cuthrell, R. E., J. Appl. Phys. 49(1), 432 (1978).

24. Chen, T. J. and Knapp, W. J., J. Amer. Cer. Soc., Discussions and Notes, 225, March-April (1980).

25. Kuan, T. S., Shih, K. K., Van Vechten, J. A. and Westdrop, W. A., J. Electrochem. Soc.: Solid State Science and Technology 127(6), 1387 (1980).

26. Slicing of Silicon Into Sheet Material, Varian Assoc., DOE/JPL 954374-10, Final Report, Sept. 1979.

27. Danyluk, S. and Reaves, R., Wear, 77 (1982) 81.

28. Chen, C. P. and Leipold, M., Amer. Cer. Soc. Bull. 59(4) (1980) 469.

29. Leighton, Orr, Mater. Res. and Stand. Jan (1972) 21.

30. J. J. Mecholsky Jun, S. W. Freiman, R. W. Rice, J., Mater. Sci., 11(1976) 1310.

31. Hogland, R. G., J. Amer. Cer. Soc. 404 (1980).

32. Cook, R. R., Lawn, B. R. and Anstis, G. R., J. Mater. Sci. 17 (1982) 1108.

33. Clarke, D. R., J. Amer. Cer. Soc. 67 (1) (1984) C-15.

34. Lawn, B. R. and Evans, A. G., J. Mater. Sci. 12 (1977) 2195.

35. Marshall, D. B., Lawn, B. R. and Evans, A. G., J. Amer. Cer. Soc. 65 (11) (1982) 561.

36. Lawn, B. R., Evans A. G. and Marshall, D. B., J. Amer. Cer. Soc. 63 (9) (1980) 574.

37. Marshall, D. B., J. Amer. Cer. Soc. (1983) 127.

38. Lankford, J. and Davidson, D., J. Mater. Sci. 14 (1979) 1662.

39. Lankford, J., J. Mater. Sci. 16 (1981) 1177.

40. Hagan, J. T., Mater. Sci. 14 (1979) 2975.

41. Lankford, J. and Davidson, D., J. Mater. Sci. 14 (1979) 1669.

42. Banerjee, R. K. and Feltham, P., J. Mater. Sci. 9 (1974) 1478.

43. Fuller, E. R., Lawn, B. R. and Cook, R. F., J. Amer. Cer. Soc. 66(5) (1983) 314.

44. Lawn, B. R., Marshall, D. B., Anstis, G. R. and Dabbs, T. P., J. Mater. Sci. 16 (1981) 2846.

45. Puttick, K. E. and Shahid, M. A., Phys. Stat. Sol. (a) 59, K5 (1980).

46. Eremenko, V. G. and Nikitenko, V. I., Phys. Stat. Sol. (9) 14, 317 (1972).

47. Hill, M. J. and Rowcliffe, D. J., J. Mater. Sci., 9 (1974) 1569-1576.

48. Renninger, M., J. Appl. Cryst. 5 (1972) 163.

49. Badrick, A. S. T., Puttrick, K. E. and El-Deghaidy, F. H. A., J. Phys. D. Appl. Phys. (1979) 909.

50. Badrick, A. S. T., El-Deghaidy, F. H. A. Puttick, K. E. and Shahid, M. A., J. Phys. D: Appl. Phys. 10 (1977) 195.

51. Hu, S. M., J. Appl. Phys. 46 (4) (1975) 1465, J. Appl. Phys. 46 (4) (1975) 1470.

52. St. John, C., Phil. Mag 32 (8) (1975) 687.

TABLE I

Summary of the Changes of Surface Hardness of Silicon

Reference	Effect	Percent Softening	Comments
Kuczynski and Hockman	Photon irradiation	70% softening	Microhardness test: Intensity and surface preparation influence the results
Ablova	H_2O adsorption	Softening	Microhardness test: Surface preparation and impurity content influence the results
Westbrook and Gilman	Potential between indenter and crystal	60% softening	Microhardness test: Effect disappeared at elevated temperatures
Yost and Williams	NaCl and Na_4P_2O	80% softening	Microhardness test; Zeta-potential measurements of crushed silicon
Cuthrell	CCl_4 and H_2O	Not determined	Surface morphology depended on fluid

Table II

Differences (percent) in Wear Rate of (100 n-type Cz Silicon
br
Compared to H_2O at P = 0.49 N

	Rabinowicz $(dA/dt)d(1/H)$	Evans $(dA/dt)\ (1/K_{I_c}{}^{2/3}\ H^{1/2})$	Experimental Value
Ethanol	50	84	56
Methanol	38	--	30
Acetone	38	67	35

TABLE III

Comparison of Mirror Constant and K_{I_c} in Ethanol, Acetone and Air

Fluids	Mirror Constant ($MN/m^{3/2}$)	K_{I_c} ($MN/m^{3/2}$)
Ethanol	2.07	0.73
Acetone	2.43	0.85
Air	5.08	1.78*

*0.95 $MN/m^{3/2}$ reference [21]

LIST OF FIGURES

grooves formed in methanol when the normal force is varied.

Figure 17 Cross-sectional area ($x10^{-9}$ m^2) versus abrasion time (s) for grooves formed in ethanol when the normal force is varied.

Figure 18 A comparison of experimental and calculated cross-sectional areas for the four fluids when P = 0.15 N.

Figure 19 A comparison of experimental and calculated cross-sectional areas for the four fluids when P=0.49N.

Figure 20 Abrasion rate versus force on the pyramidal diamond.

Figure 21 A schematic of the time sequance of the wear process. The damage zone is extended after each pass by the diamond.

Figure 22 A schematic of the wear process.

Figure 23 Hardness (Pa) versus dielectric constant of (100) n-type and (111) p-type single crystal silicon. The load on the indenting diamond was varied from 0.15-9.8 N.

Figure 24 Hardness (Pa) versus dielectric constant of (111) p-type single crystal silicon. The load on the indenting diamnd was varied from 0.15-9.8 N.

Figure 25 Optical micrographs of a typical Vickers indentation in (100) p-type silicon. The indentation was made while the silicon was immersed in 10^{-3} M/ℓ NaI solution. The loads on the diamond were (a) 9.8N (b) 4.9N and (c) 2.94N.

Figure 26 Optical micrographs of a typical Vickers indentation in (111) p-type silicon indented in 10^{-3} M/ NaI solution. The loads on the diamond were (a) 9.8N (b) 4.9N (c) 2.94N and (d) 1.96N.

Figure 27 Variation of Hardness versus immersion time in a fluid. In this case the fluid was 100ppm $CaCl_2$ and the indentation load was 0.49N.

Figure 28 Microhardness ($x10^9$ Pa) versus salt concentration (ppm) for (100) p-type silicon indented in NaCl, $CaCl_2$ and $FeCl_3$.

Figure 29 Microhardness ($x10^9$ Pa) versus salt concentration (ppm) for (100) n-type silicon indented in NaCl, $CaCl_2$ and $FeCl_3$.

Figure 30 Microhardness versus load (N) for (111) p-type C_z silicon indented in 10^{-3} M/1 NaI.

Figure 31 Vickers indentation (P=0.49N) in (100) n-type Cz silicon (a) unetched (b) etched. The indentation was made in de-ionized water containing $1.7x10^{-3}$ M/ NaCl.

Figure 32 Vickers indentations (P=0.49N) in (111) p-type Cz silicon. The

indentations were carried out in (100) ppm NaCl, NaBr and NaI.

Figure 33 Variation of crack length c vs. NaI concentration.

Figure 34 Variation of damage zone D with NaI concentration.

Figure 35 Plot of length of damage zone (D) as a function of indentation load (gf) for (111) p-type silicon indented in 10^{-3} M/l NaI.

Figure 36 Plot of the crack length, C, versus the load P for (111) p-type silicon indented in 10^{-3} M/l NaI.

Figure 37 Three-point bend test for determination of fracture strength of silicon. A linear multi-scratch groove is formed in fluids and the fracture strength is obtained.

Figure 38 SEM micrograph of the (110) cleavage fracture surface of p-type silicon produced in three-point bending. The linear multiple-scratch groove produced by a 0.54 N dead-loaded pyramid diamond is shown in the cross section. The bend test is conducted in air. Shown in the figure is the groove, mirror and hackle region.

Figure 39 Bending strength (Nm^{-2}) versus groove area$^{1/2}$ (m) of silicon fractured in air. The fluids listed refer to a linear groove that was formed on the (100) surface in the presence of those fluids. The strength is expected to decrease with groove area. The surface mechanical properties are apparently dominated by either the plastic zone or microcracks beneath the groove.

Figure 40 The bending strength versus mirror distance for three-point bend test of (100) p-type silicon. The mirror distance is linear with d_m-1/2. It was expected that all the slopes would be equal if the fluid influenced the depth of the groove and not the surface mechanical properties of silicon. The relation of the σ_f and d_m is $\sigma_f d_m 1/2 = A$ where A is a constant for each fluid.

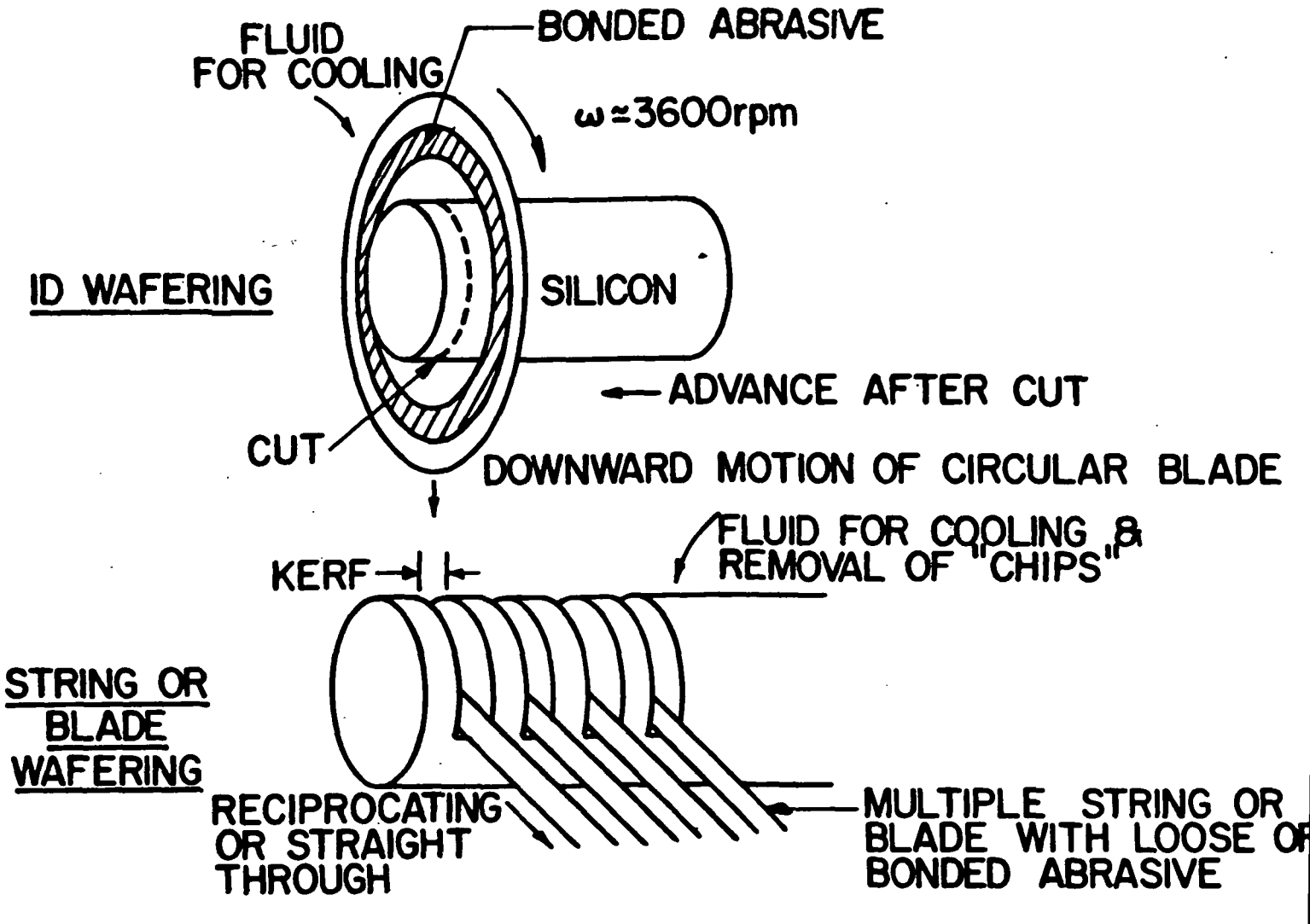

Figure 1 A schematic diagram of two wafering processes.

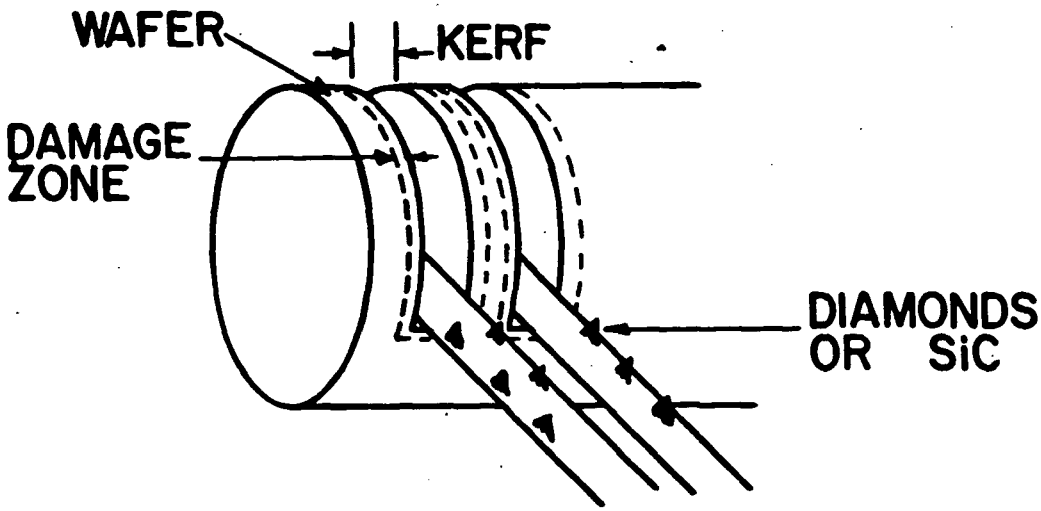

Figure 2 A schematic diagram of the string wafering process.

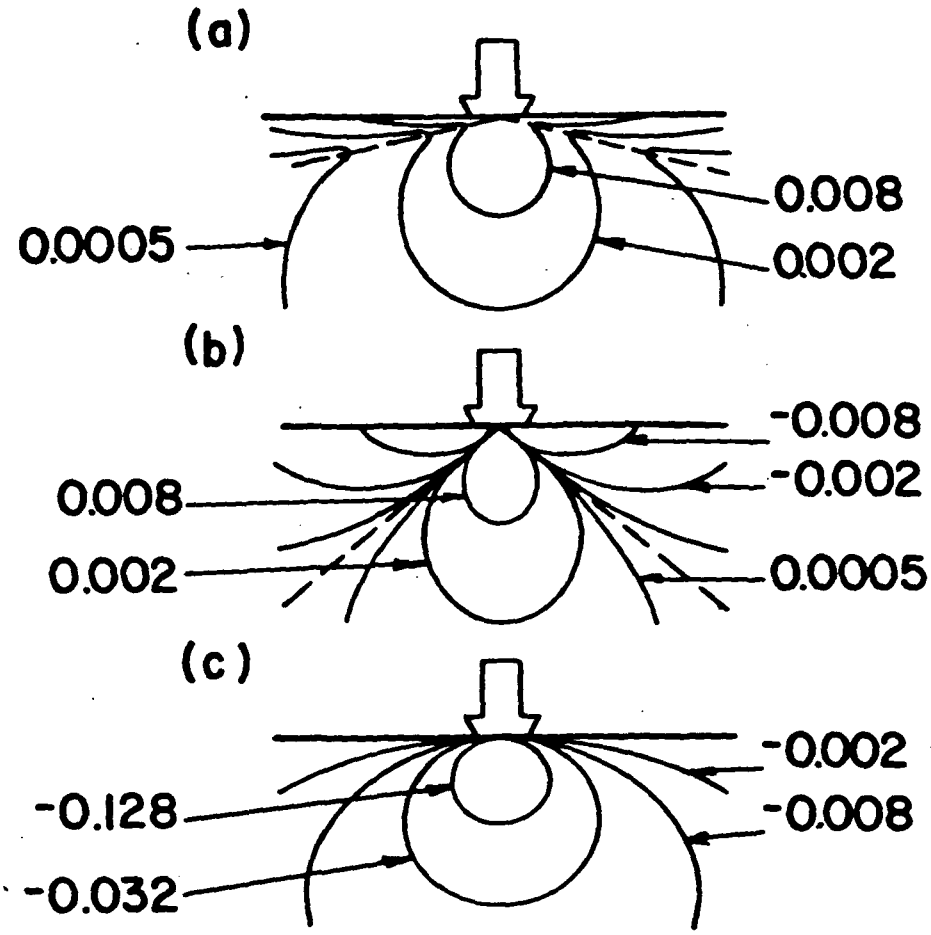

Figure 3 Contours of principal normal stresses (a) σ_{11} (b) σ_{22} and (c) σ_{33} shown in the plane containing the stress axis.

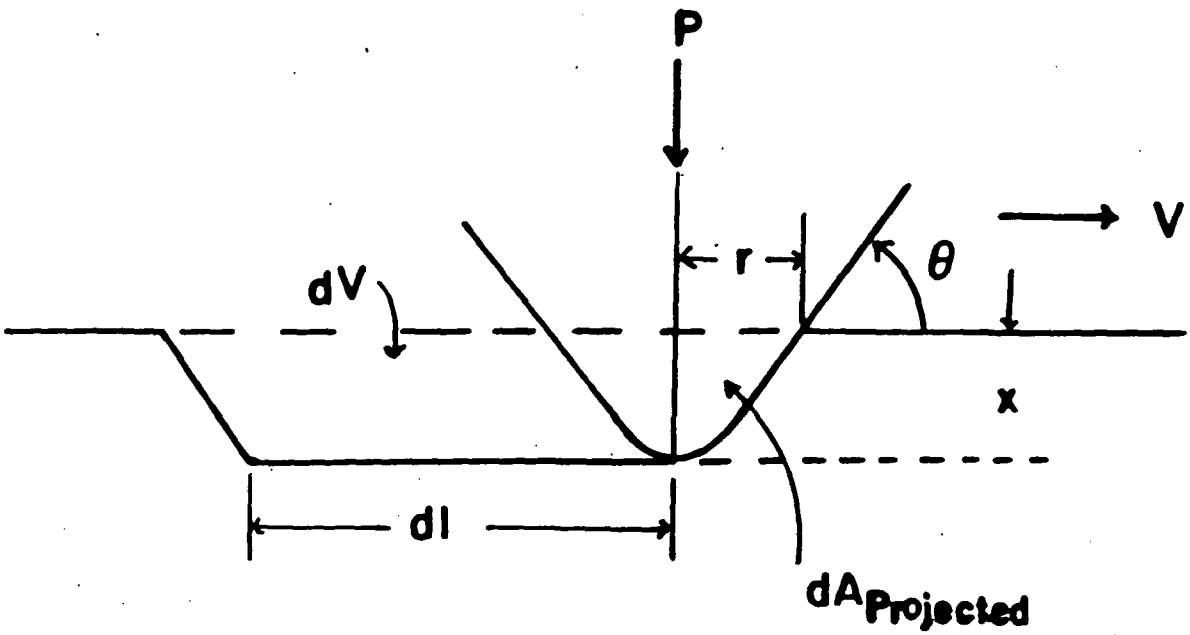

Figure 4 Schematic diagram of a conical indentor sliding on a brittle solid.

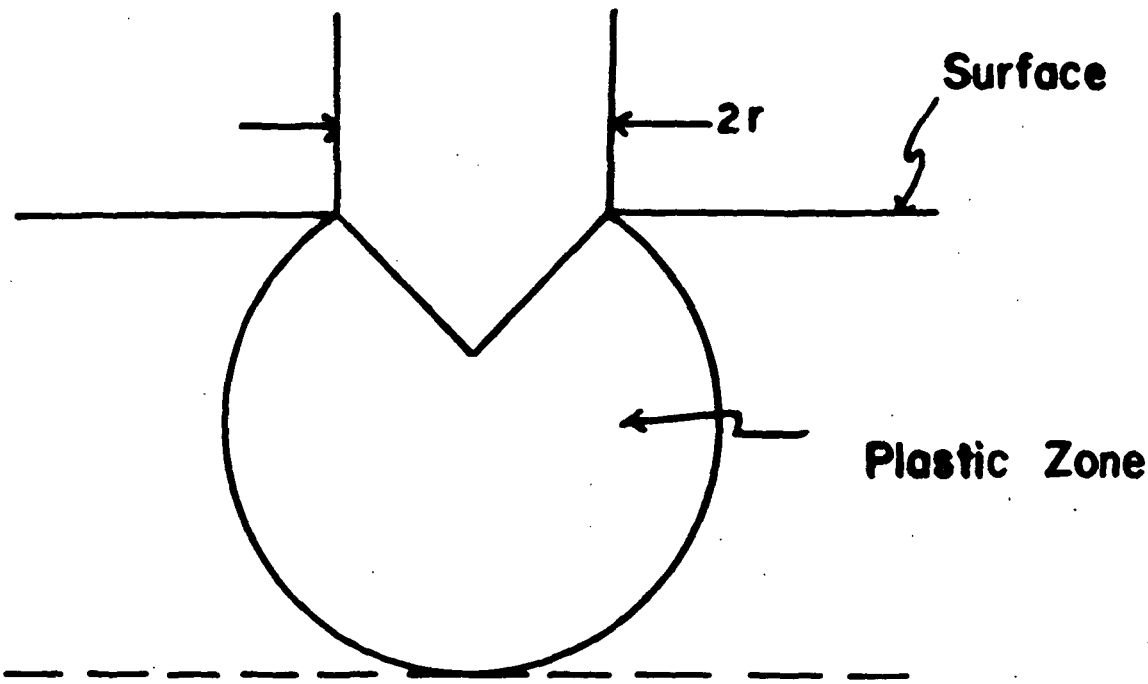

Figure 5 A schematic of the Evans model of abrasion of non-metals.

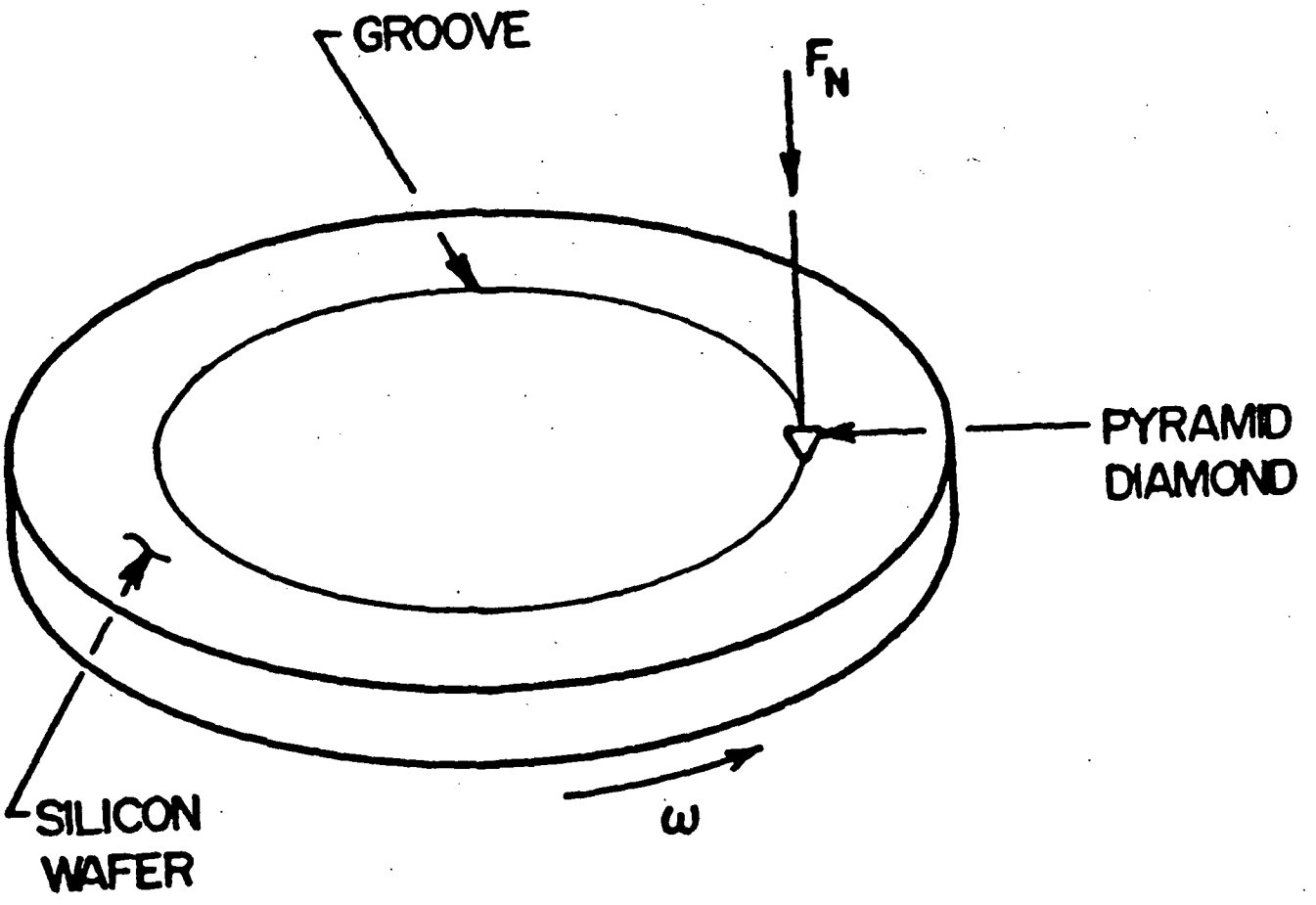

Figure 6 A schematic representation of the experiment for abrading silicon by diamond. Grooves are produced on the silicon wafer and the groove depth is measured as a function of time, fluid environment and normal force on the diamond. The surface of the silicon is examined by scanning electron microscopy (SEM) for mode of silicon removal.

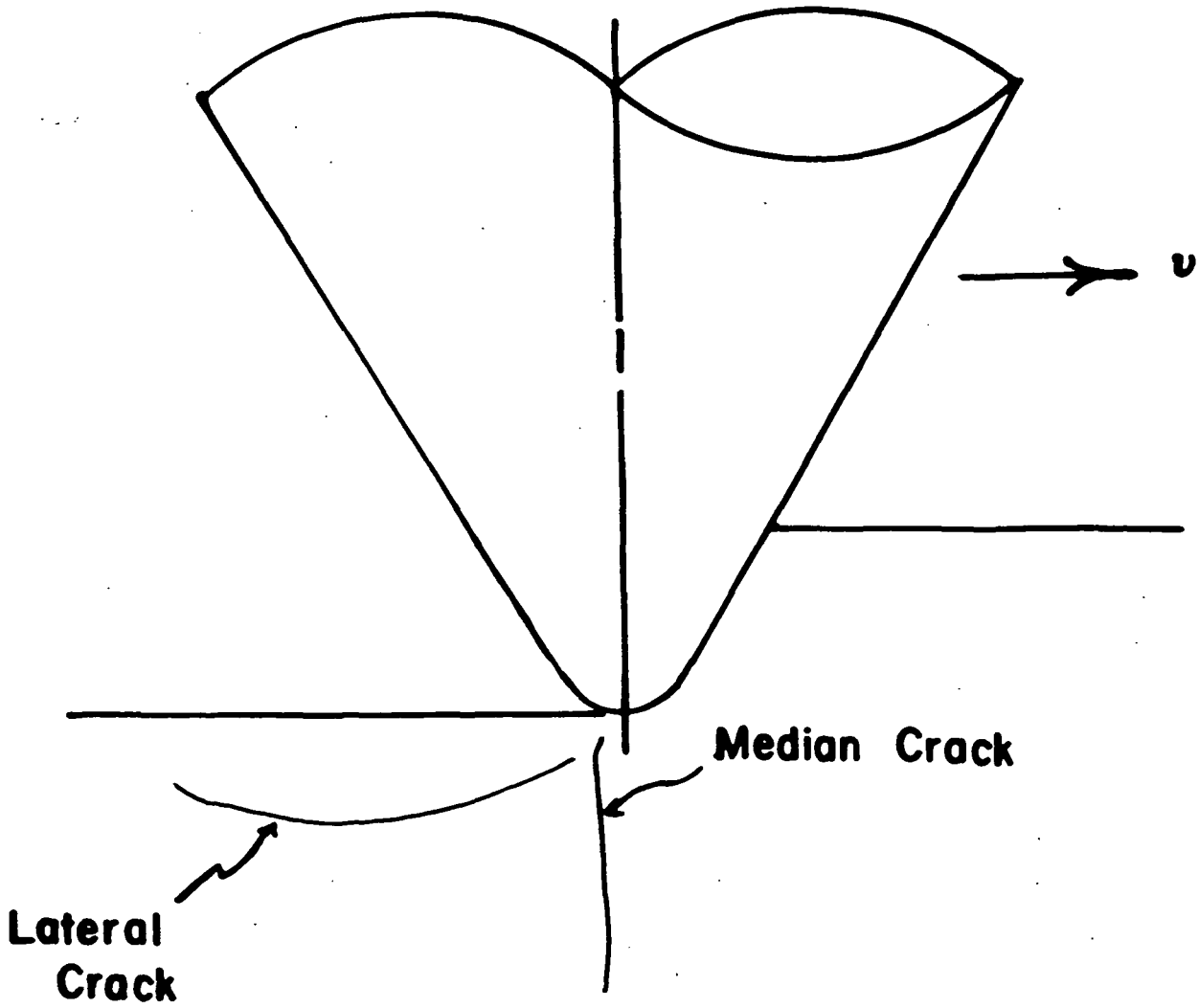

Figure 7 A schematic diagram of a moving pointed indenter and the corresponding cracks generated in the substrate.

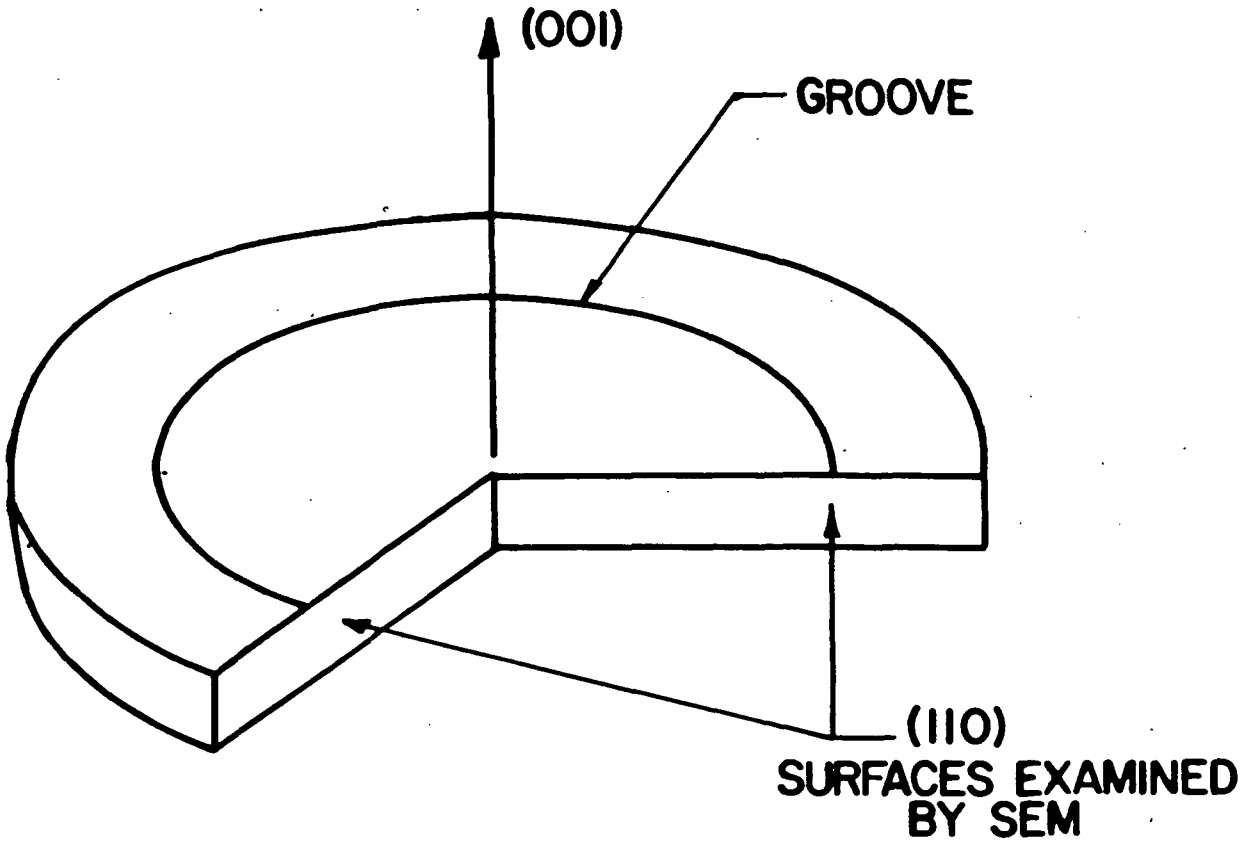

Figure 8 A schematic diagram of the location of the sections used for SEM investigations.

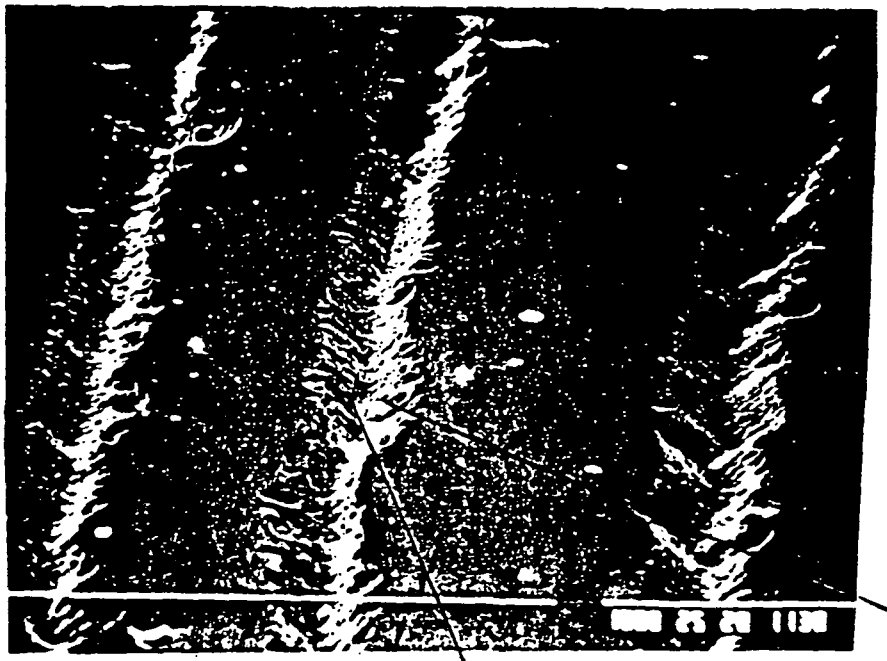

0.3, 0.6 and 1.3×10^2 s grooves; F_N = 0.2 N; Ethanol

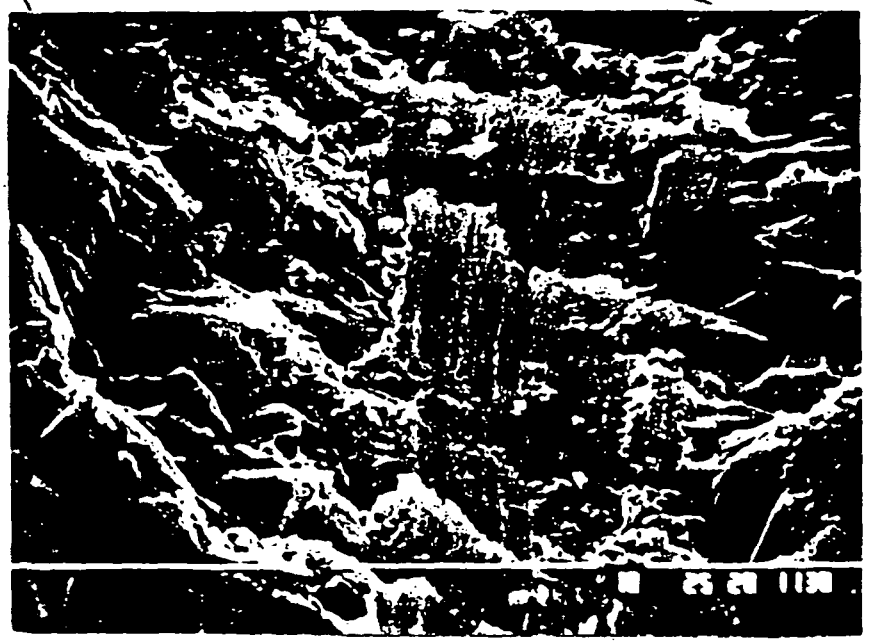

Bottom of Groove; Plastic Deformation of Protrusions $t = 0.6 \times 10^2$ s

Figure 9 Scanning electron micrographs showing the relative positions of the circular multi-scratch grooves.

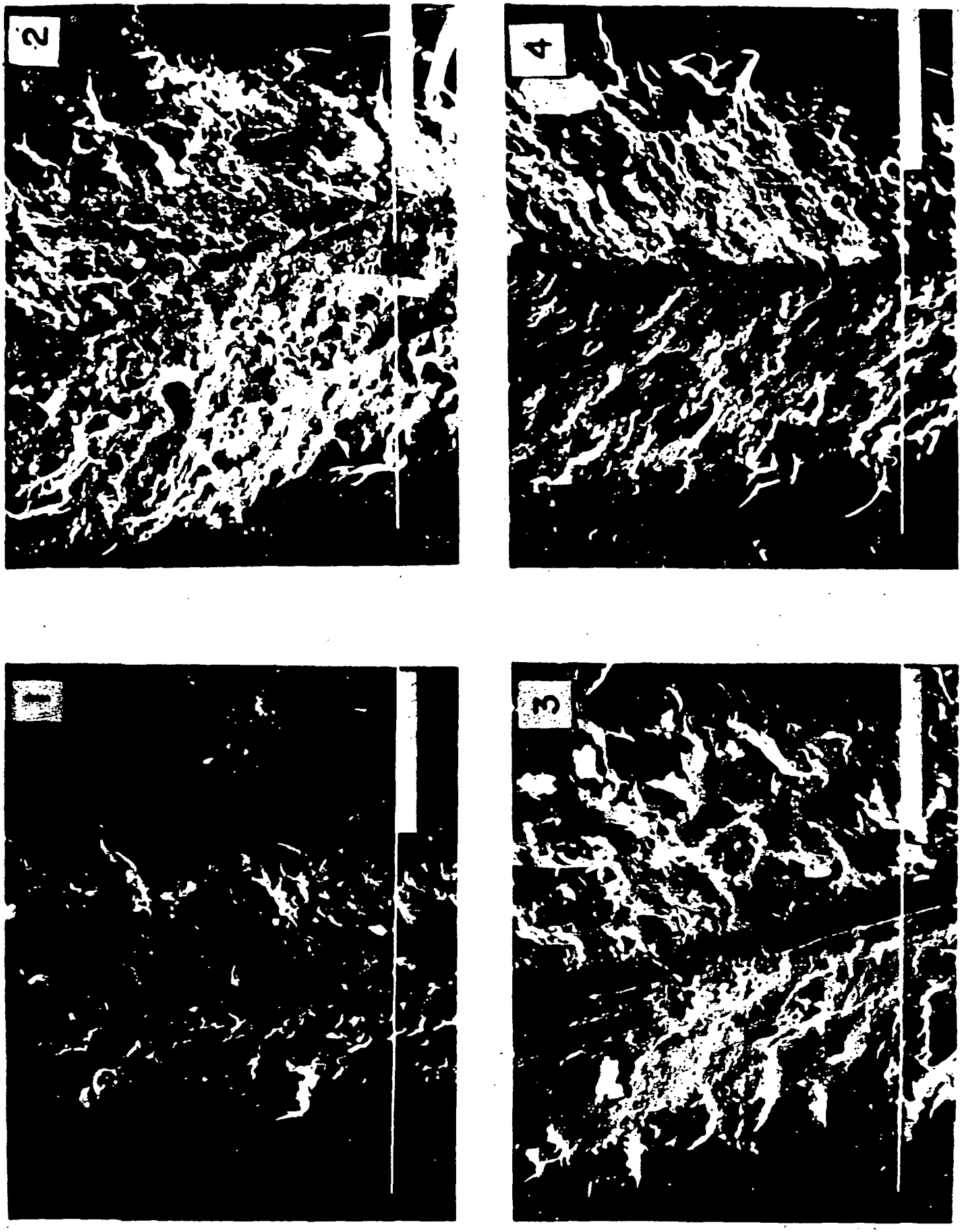

Figure 10 SEM micrographs of silicon abraded at room temperature by a 136° conical diamond in the presence of (1) de-ionized water, (2) ethanol, (3) acetone and (4) 5% NaCl + de-ionized water. The loading force was 0.098N and the abrasion time was 1.8×10^3 s, all other conditions being held constant.

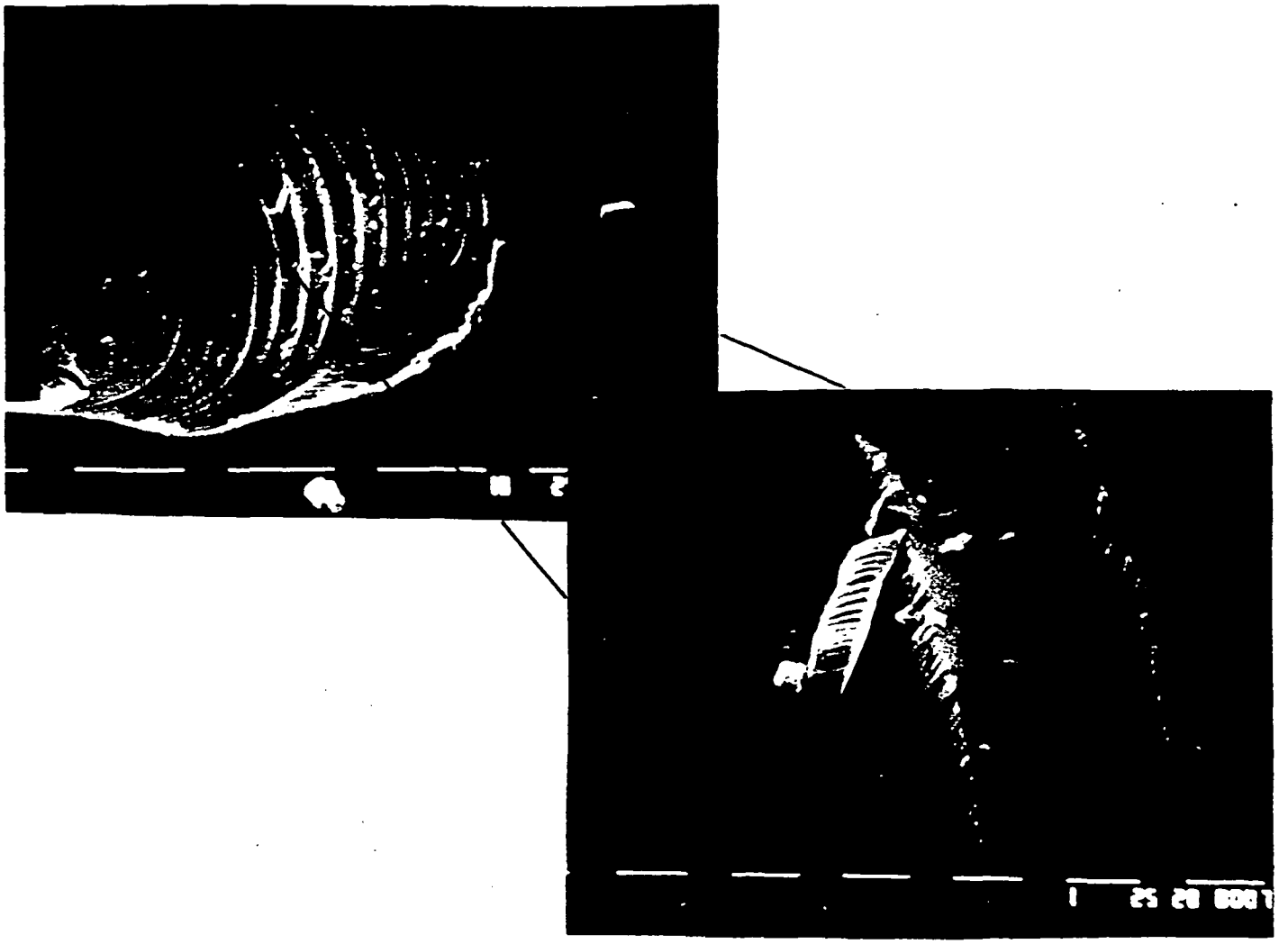

Figure 11 Scanning electron micrographs of a conchoidal fracture typically seen. A terraced structure is visible along with debris particles.

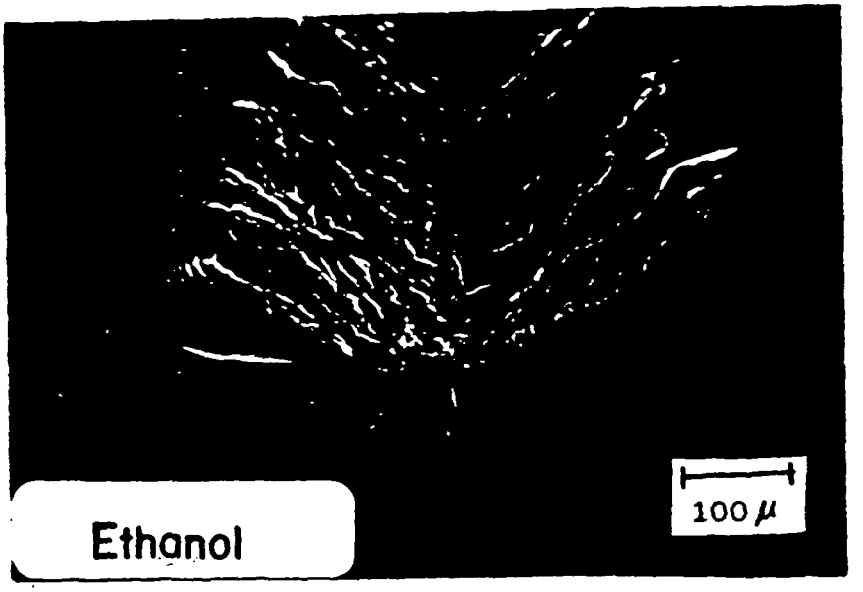

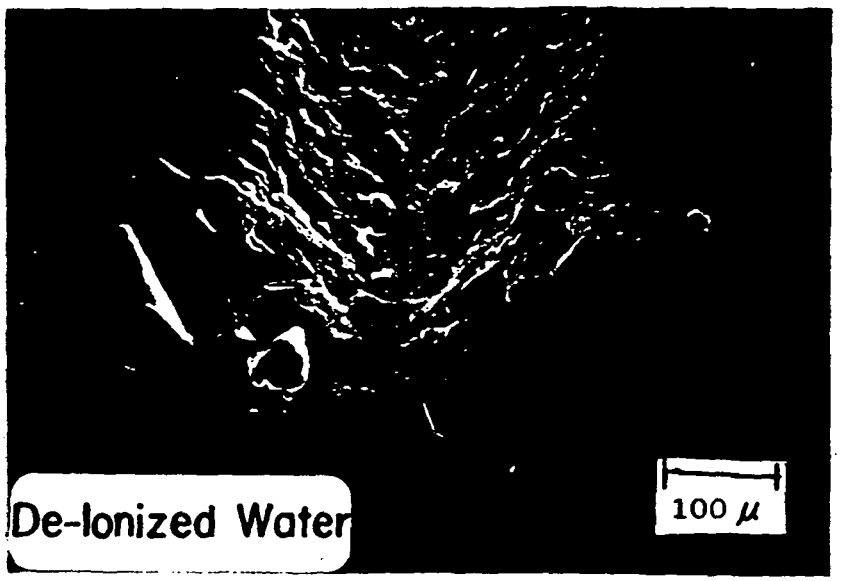

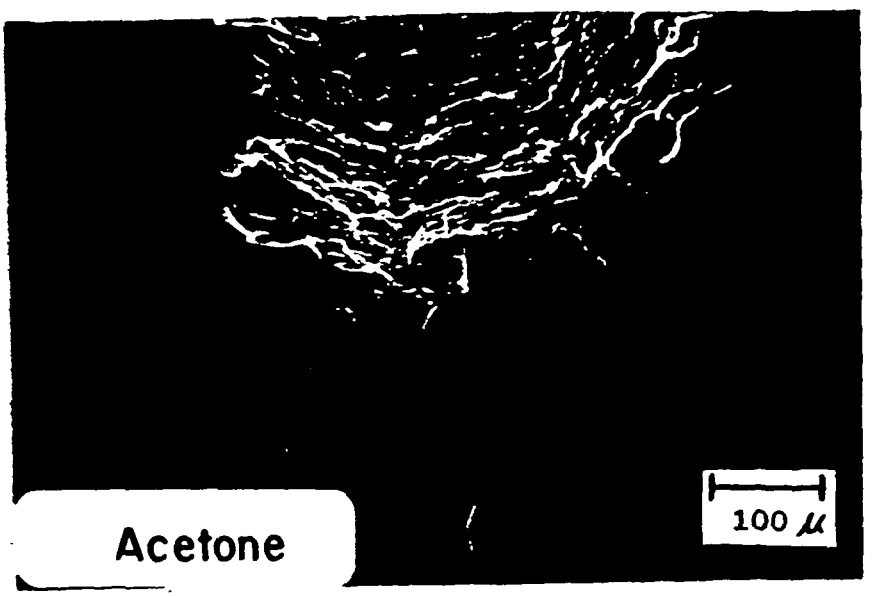

Figure 12 Scanning electron micrographs of the cross-sectional views of the (110) fracture surfaces of Cz silicon abraded in ethanol, acetone and de-ionized water.

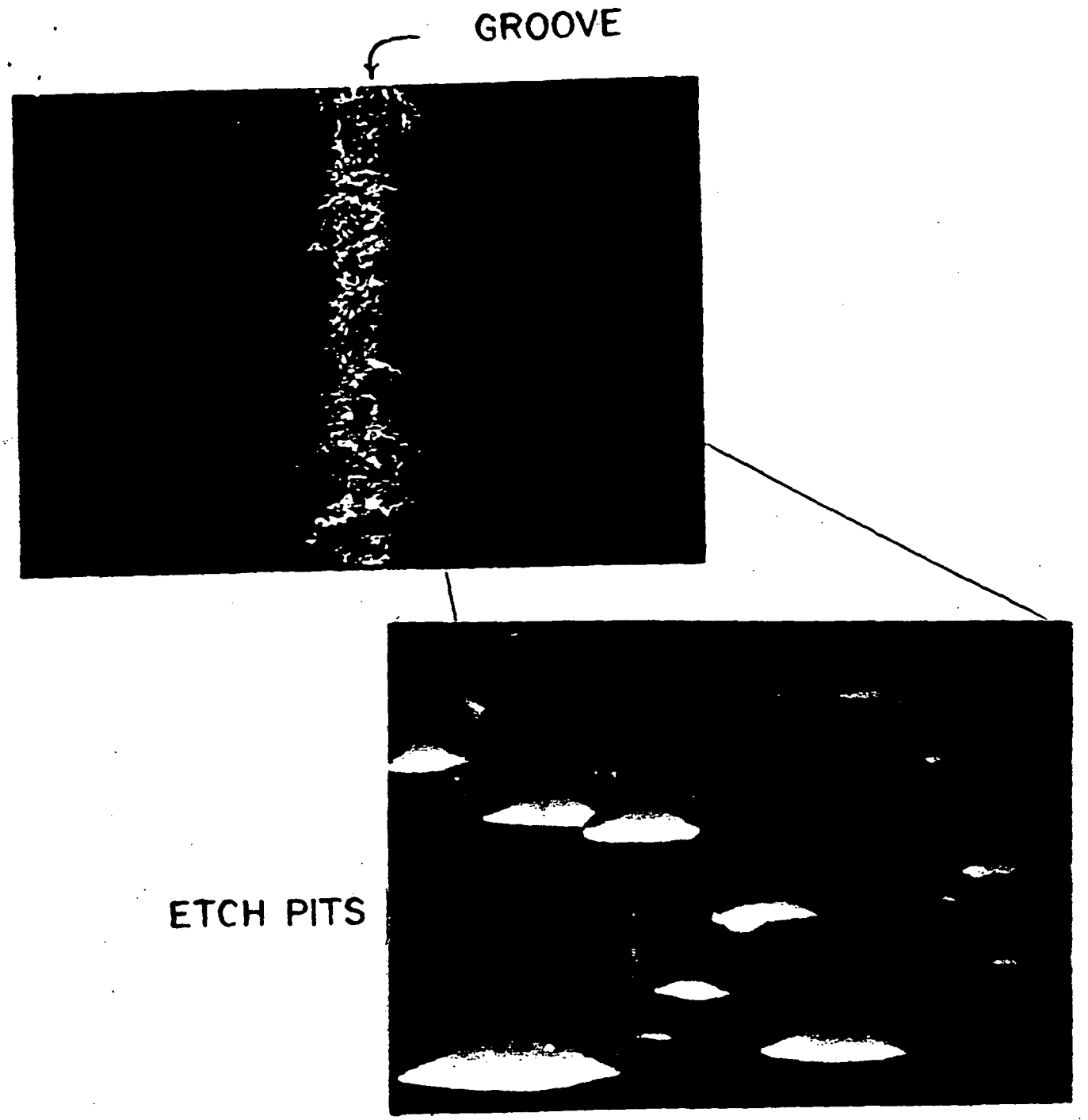

Figure 13 SEM micrographs of the (100) p-type C_z silicon abraded in ethanol and de-ionized water, annealed in N_2 at 1000°C for 30 min. and etched for in 10% Gracial Acid, HF, $3HNO_3$ solution 80 min.

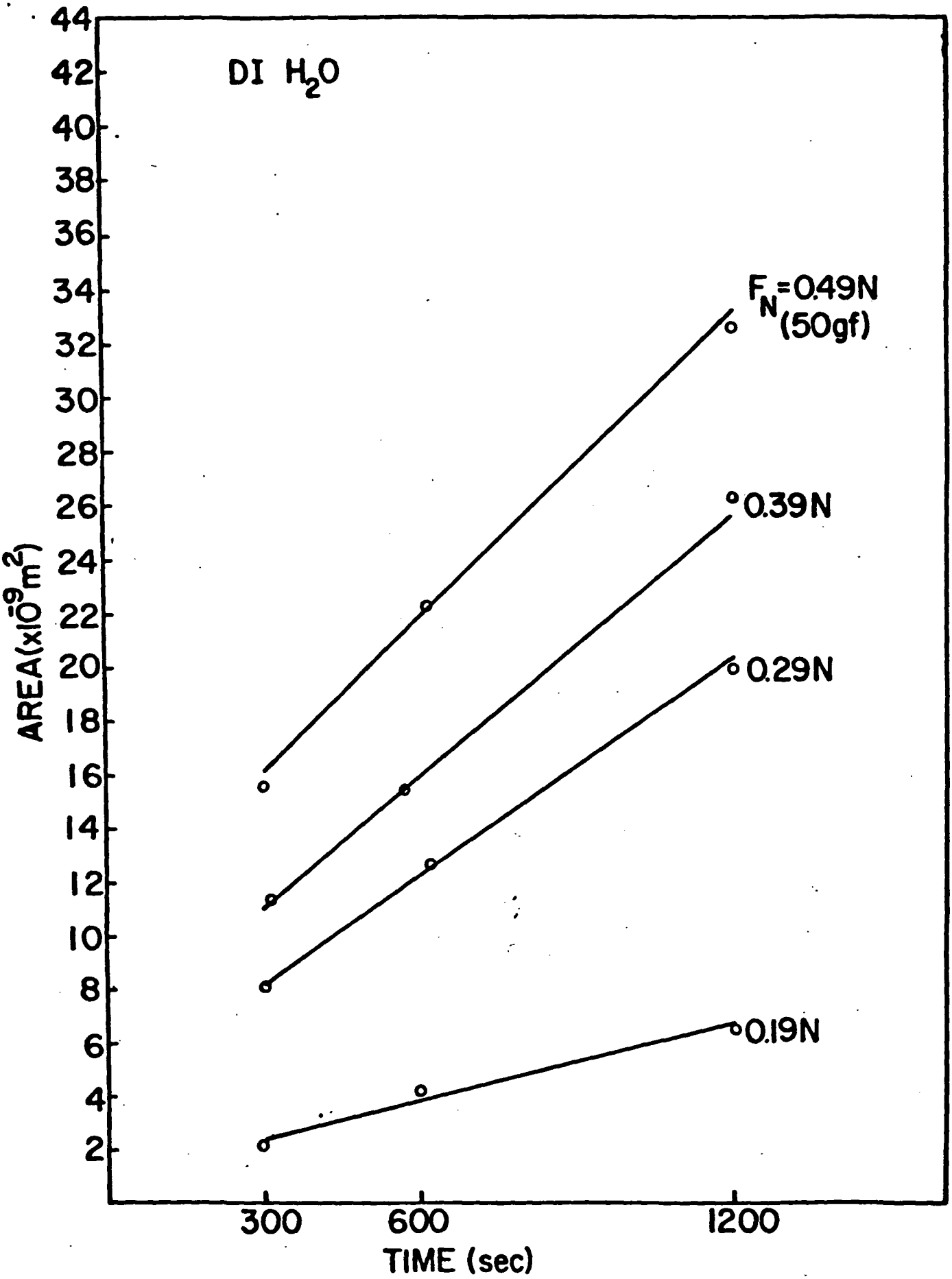

Figure 14 Cross-sectional area (x10^{-9} m^2) versus abrasion time (s) for grooves formed in de-ionized water when the normal force is varied.

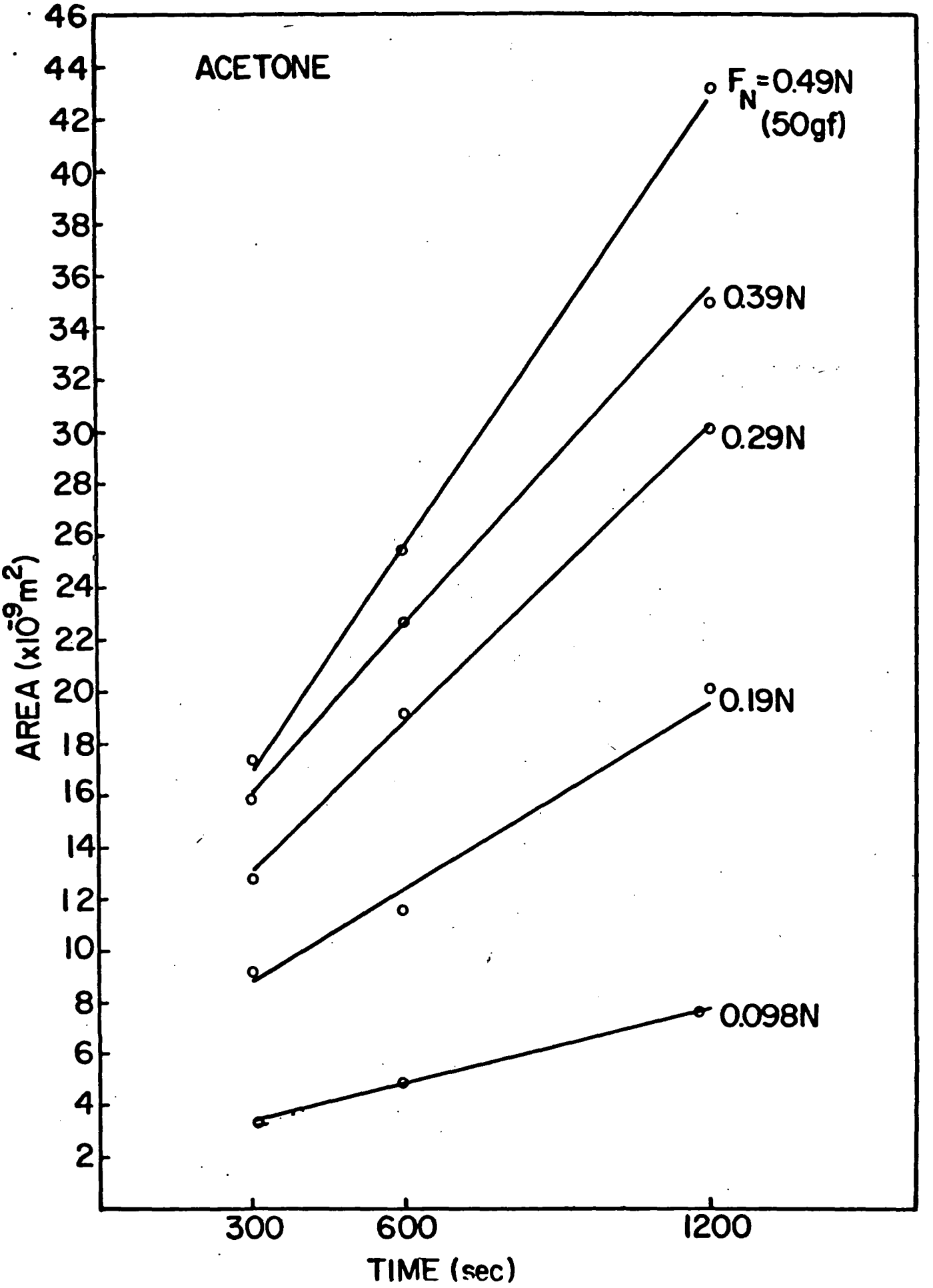

Figure 15 Cross-sectional area (x10^{-9} m^2) versus abrasion time (s) for grooves formed in acetone when the normal force is varied.

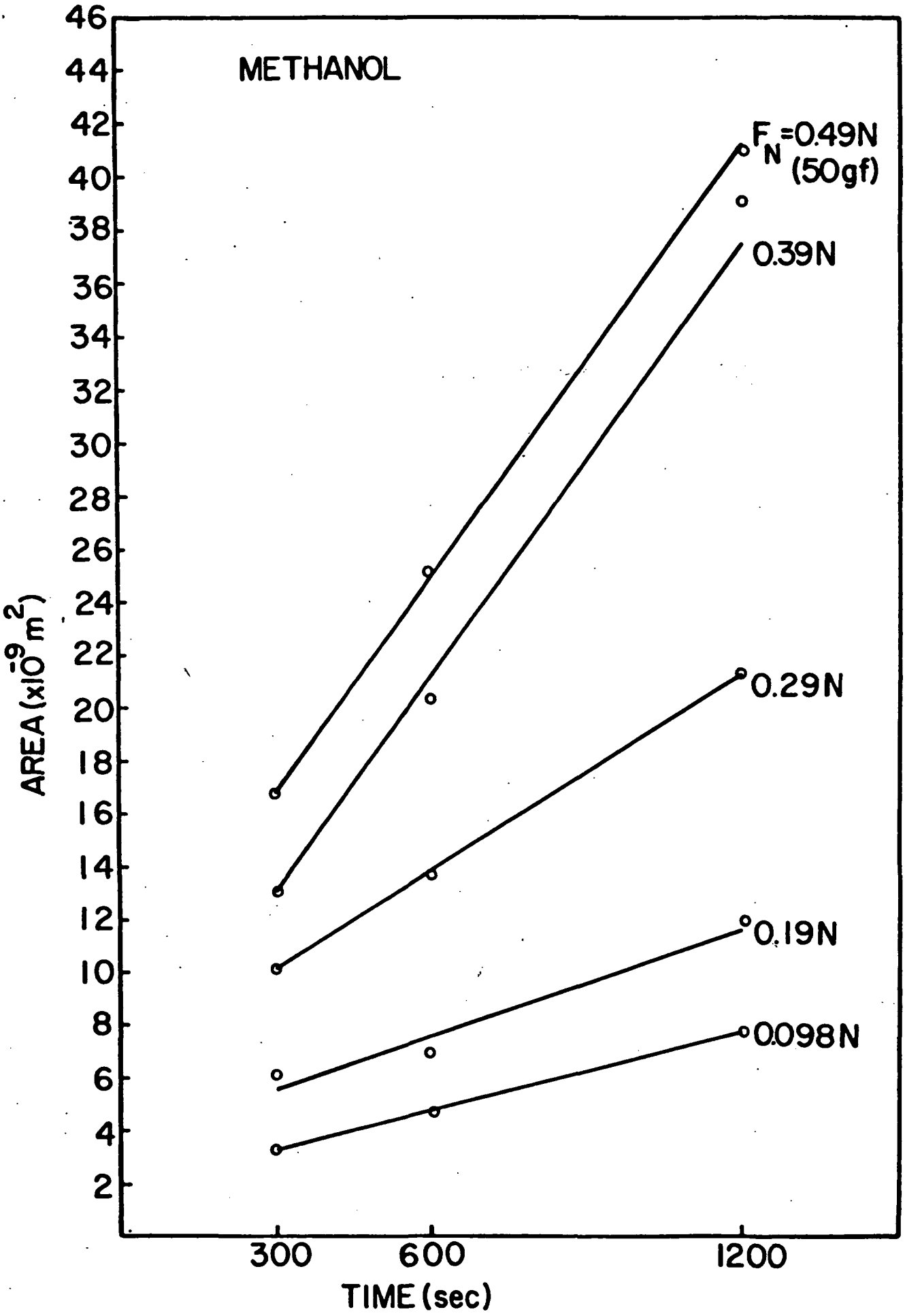

Figure 16 Cross-sectional area ($x10^{-9}$ m^2) versus abrasion time (s) for grooves formed in methanol when the normal force is varied.

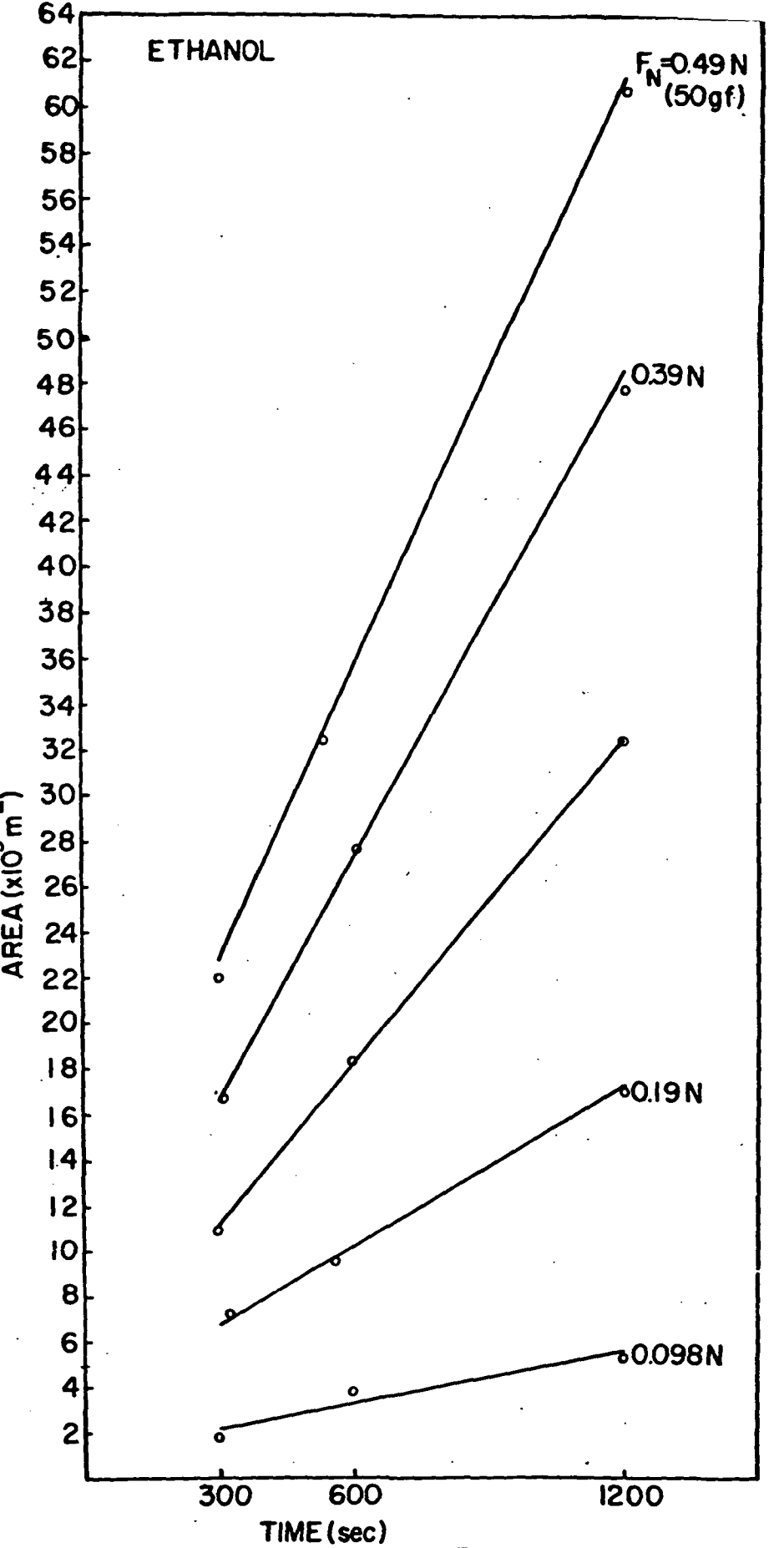

Figure 17 Cross-sectional area ($x10^{-9}$ m^2) versus abrasion time (s) for grooves formed in ethanol when the normal force is varied.

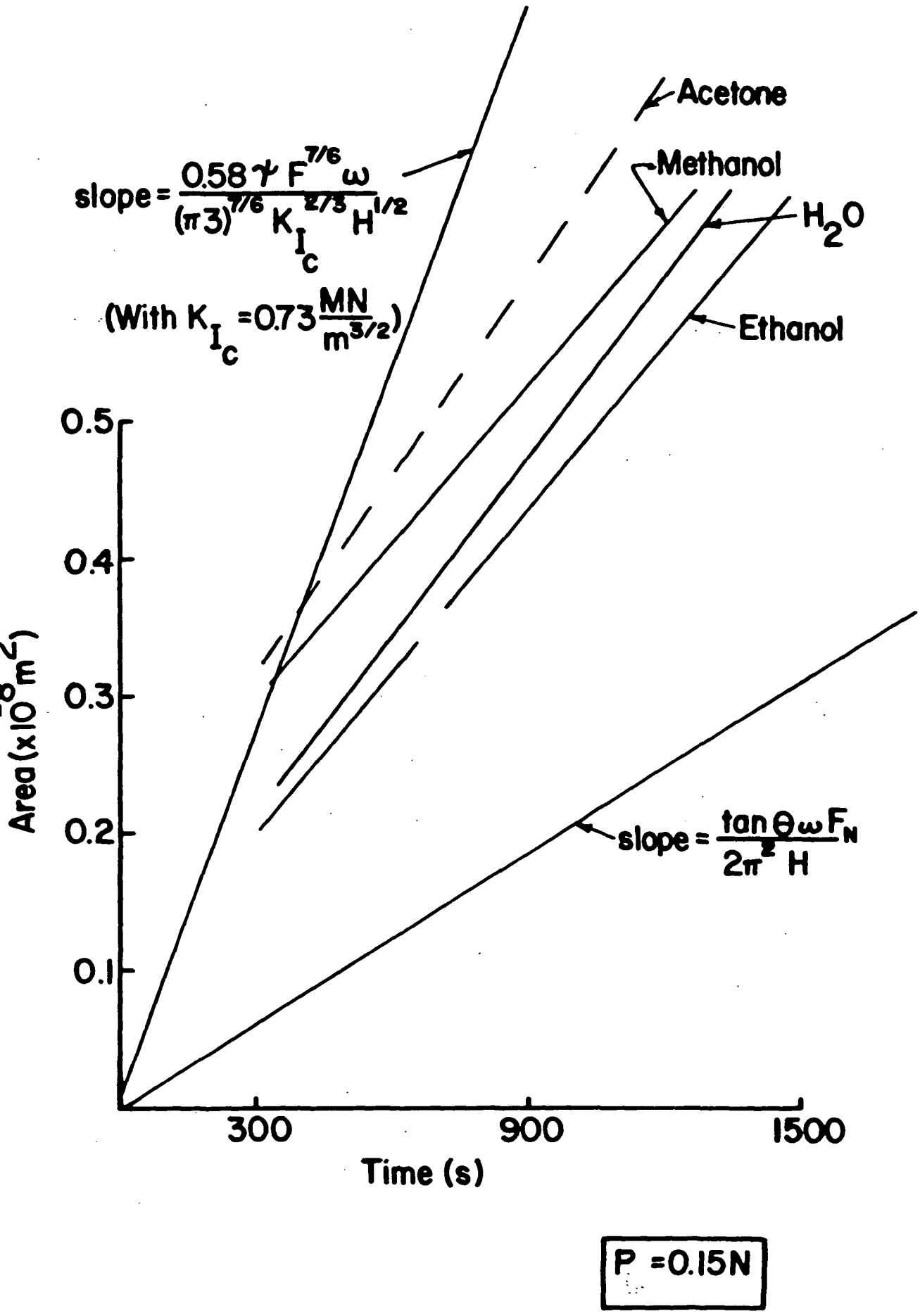

Figure 18 A comparison of experimental and calculated cross-sectional areas for the four fluids when P = 0.15 N.

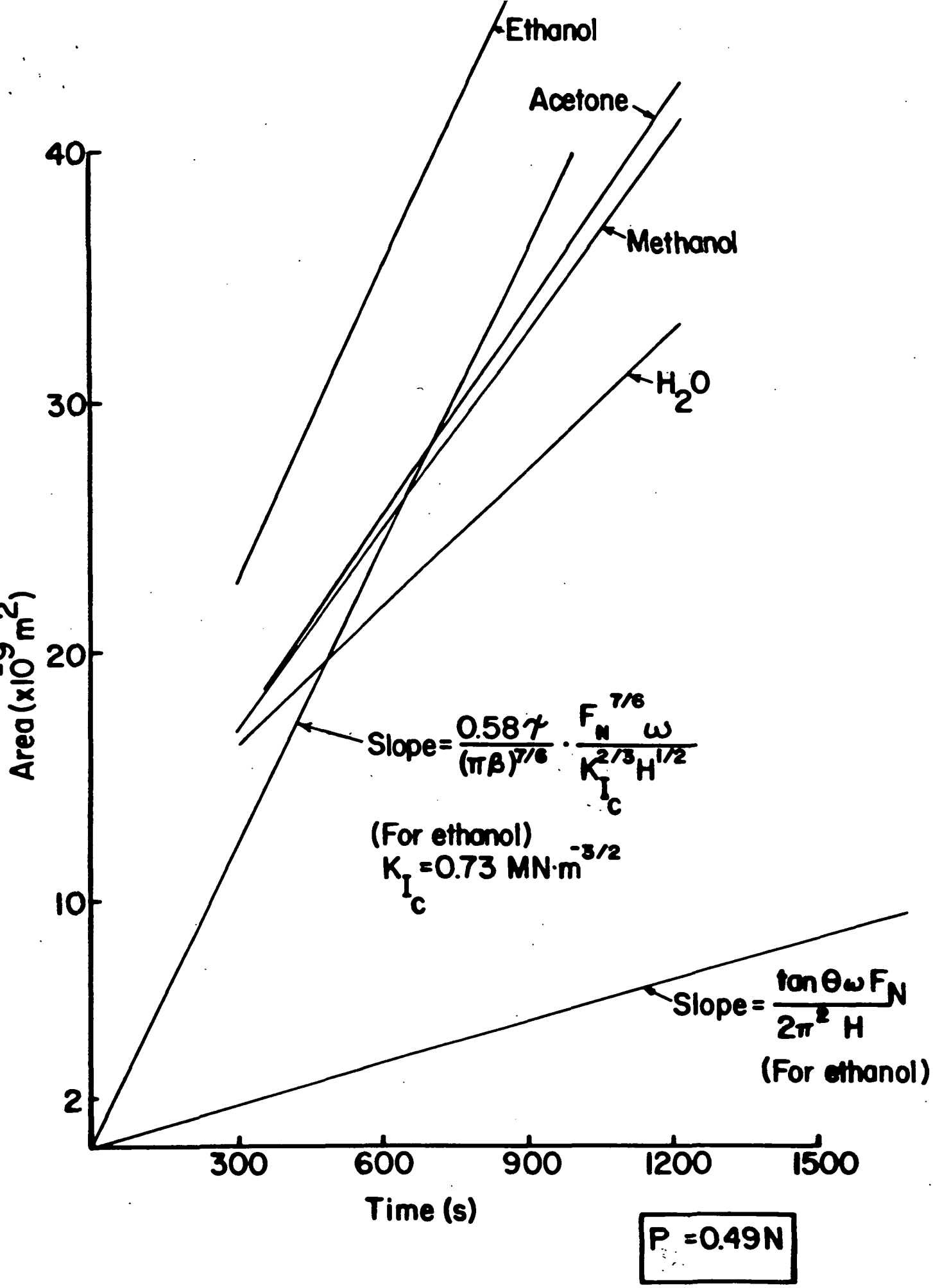

Figure 19 A comparison of experimental and calculated cross-sectional areas for the four fluids when P=0.49N.

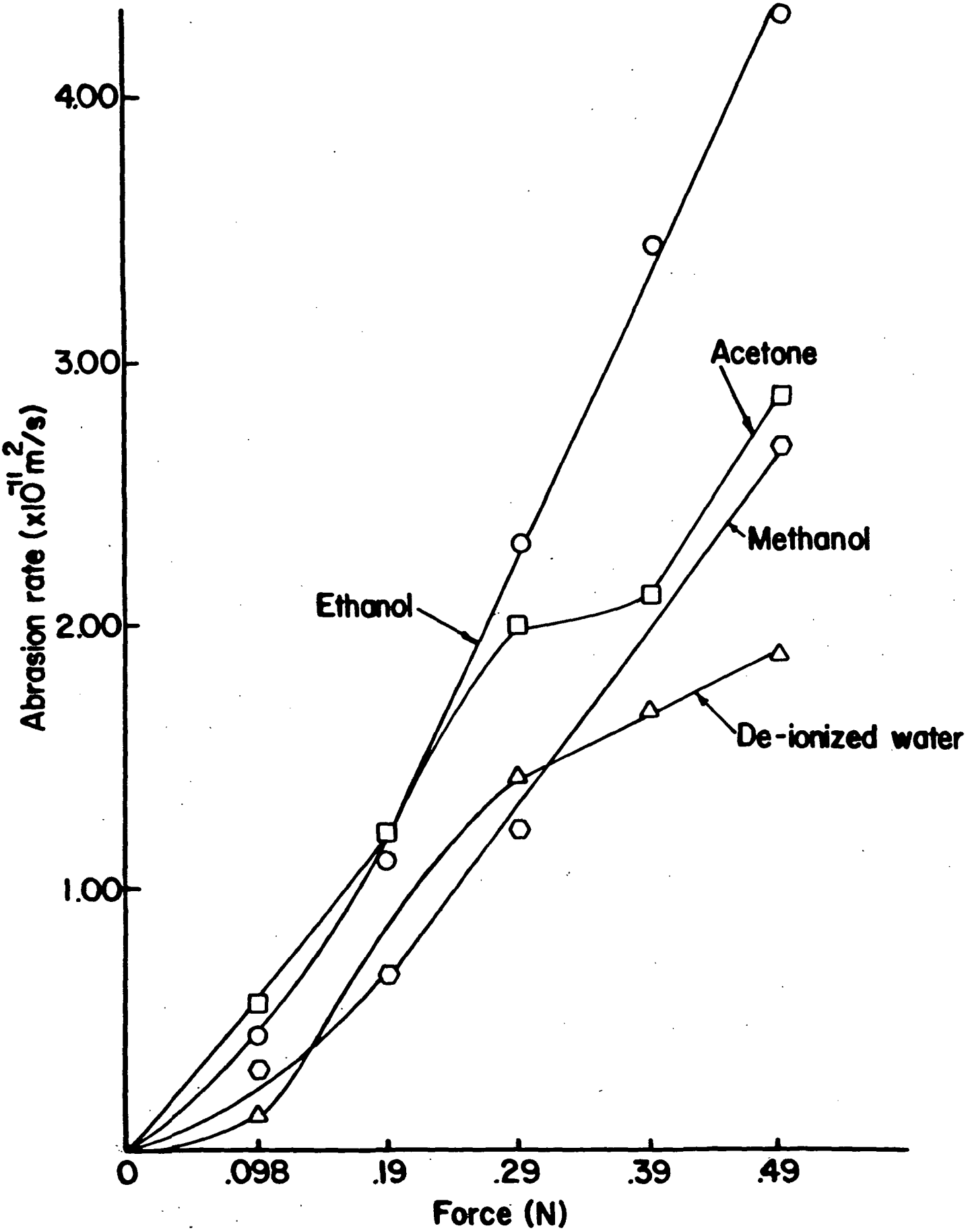

Figure, 20 Abrasion rate versus force on the pyramidal diamond.

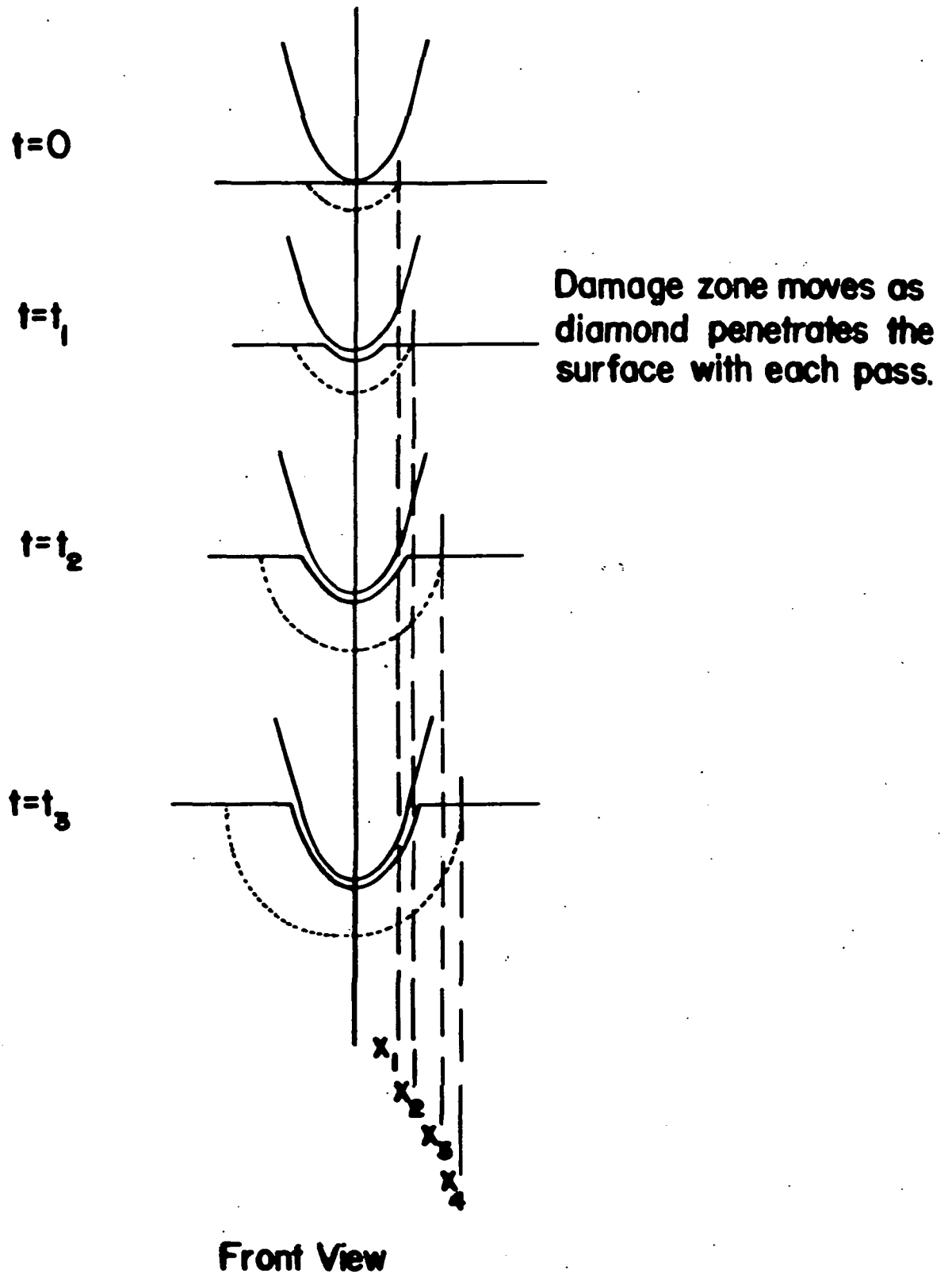

Figure 21 A schematic of the time sequance of the wear process. The damage zone is extended after each pass by the diamond.

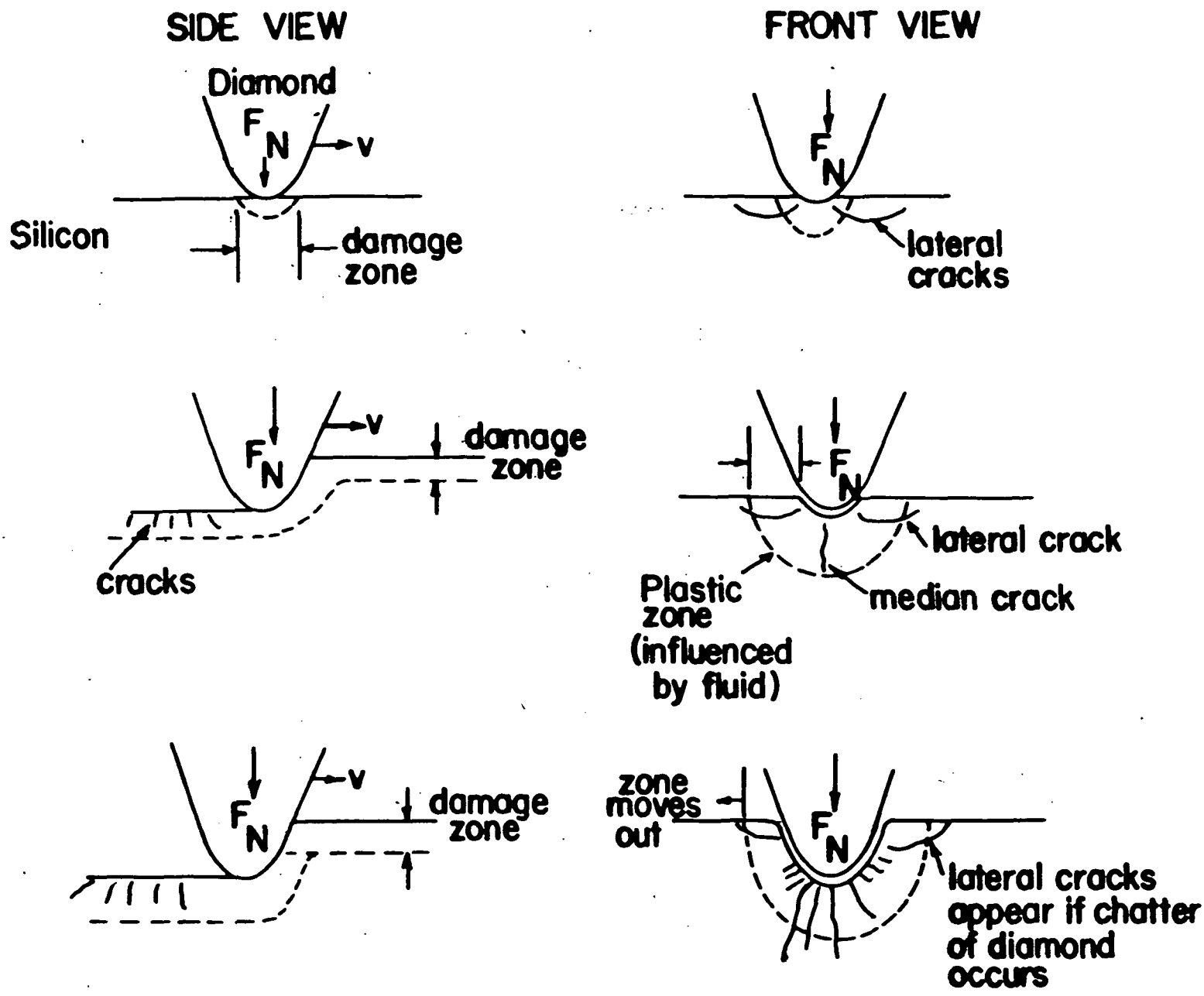

Figure 22 A schematic of the wear process.

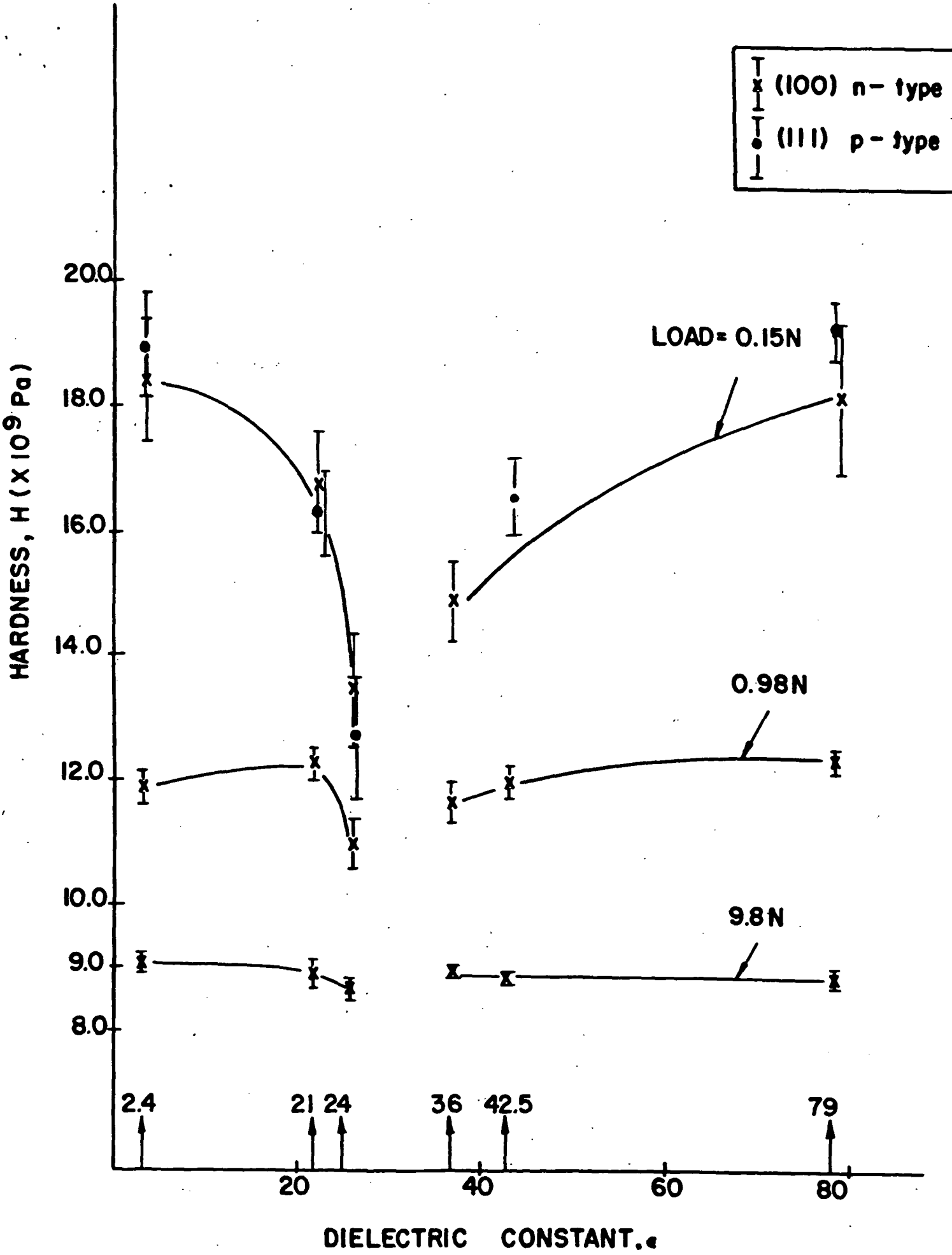

Figure 23 Hardness (Pa) versus dielectric constant of (100) n-type and (111) p-type single crystal silicon. The load on the indenting diamond was varied from 0.15-9.8 N.

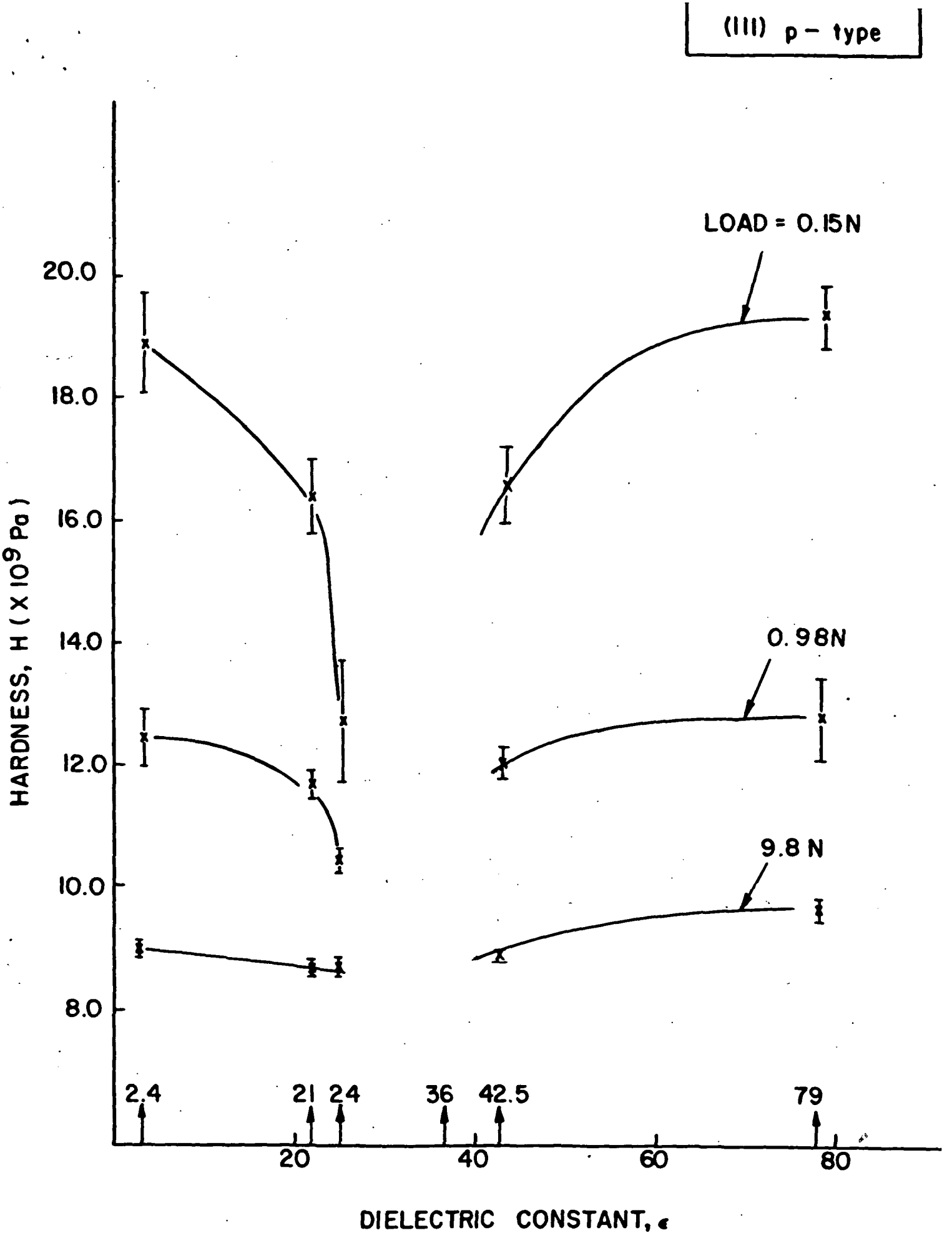

Figure 24 Hardness (Pa) versus dielectric constant of (111) p-type single crystal silicon. The load on the indenting diamnd was varied from 0.14-9.8 N.

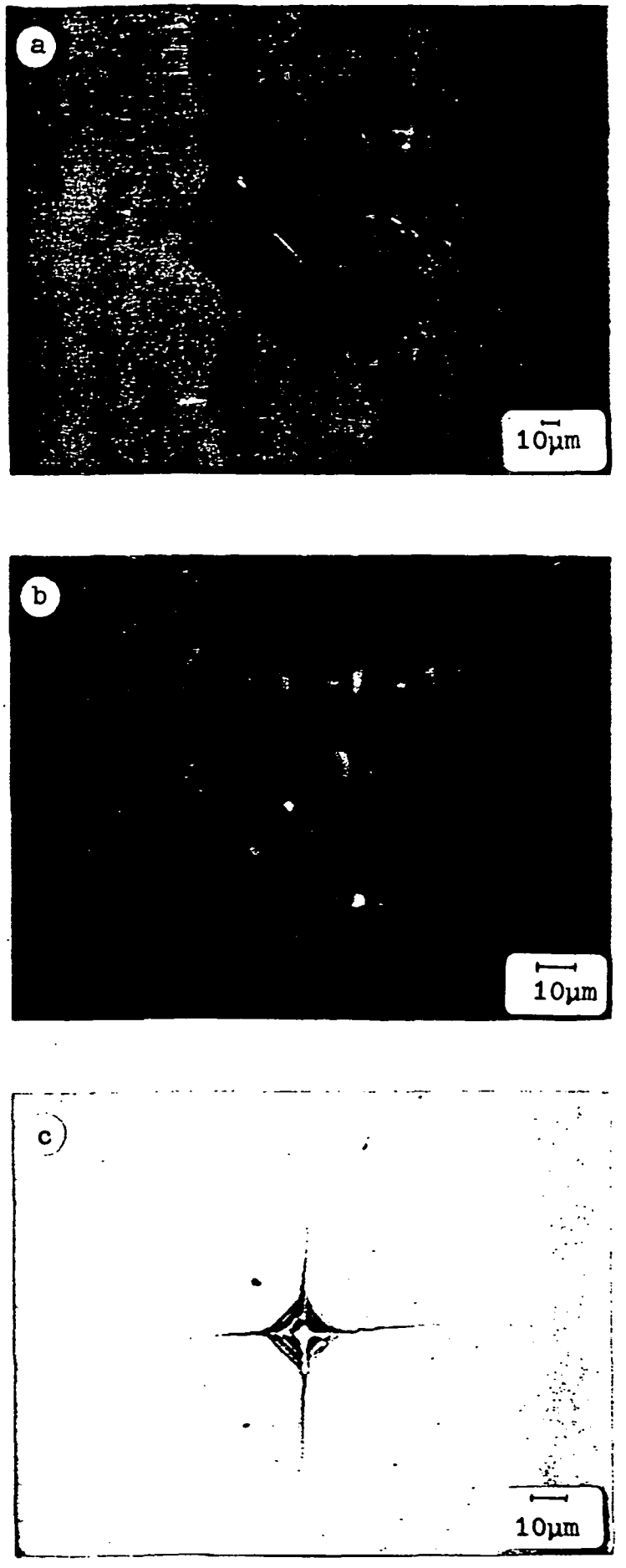

Figure 25 Optical micrographs of a typical Vickers indentation in (100) p-type silicon. The indentation was made while the silicon was immersed in 10^{-3} M/ℓ NaI solution. The loads on the diamond were (a) 9.8N (b) 4.9N and (c) 2.94N

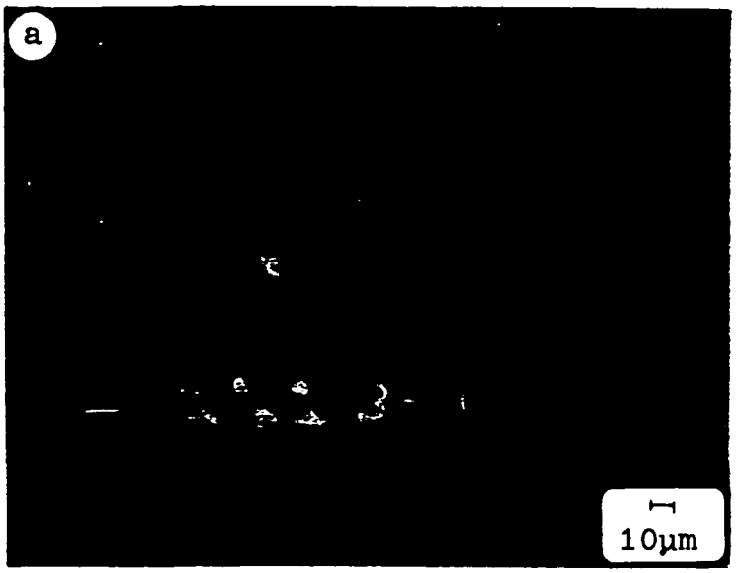

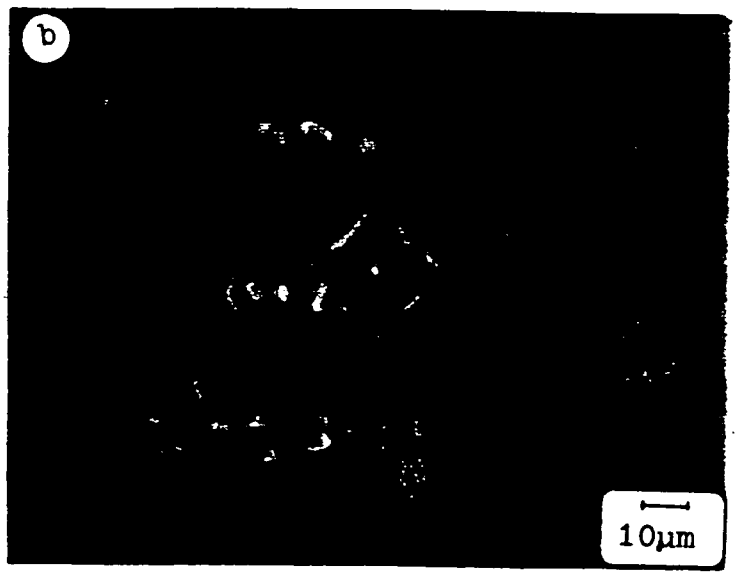

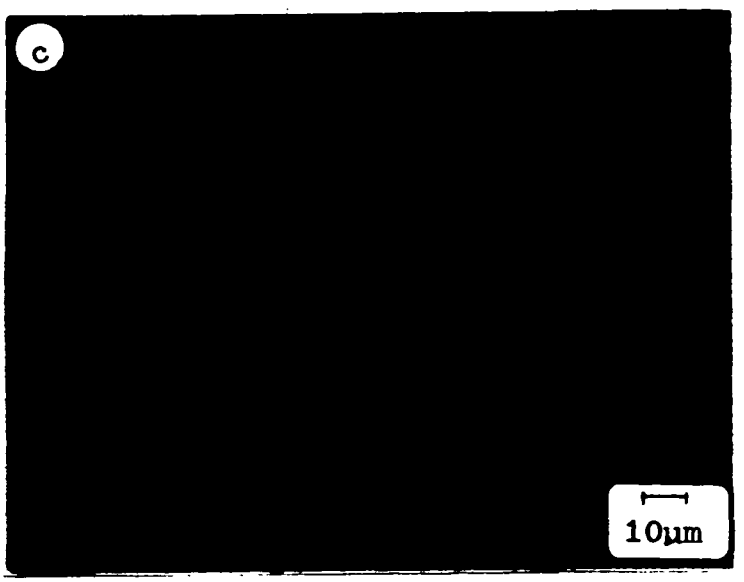

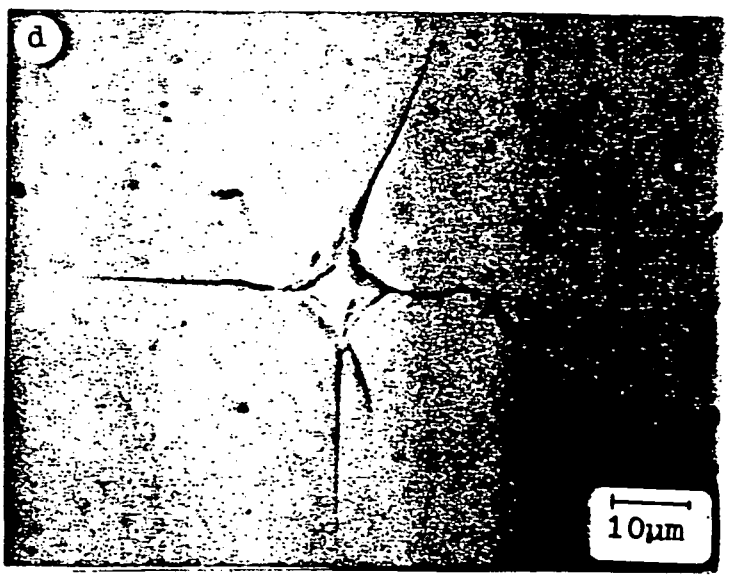

Figure 26 Optical micrographs of a typical Vickers indentation in (111) p-type silicon indented in 10^{-3} M/ NaI solution. The loads on the diamond were (a) 9.8N (b) 4.9N (c) 2.94N and (d) 1.96N.

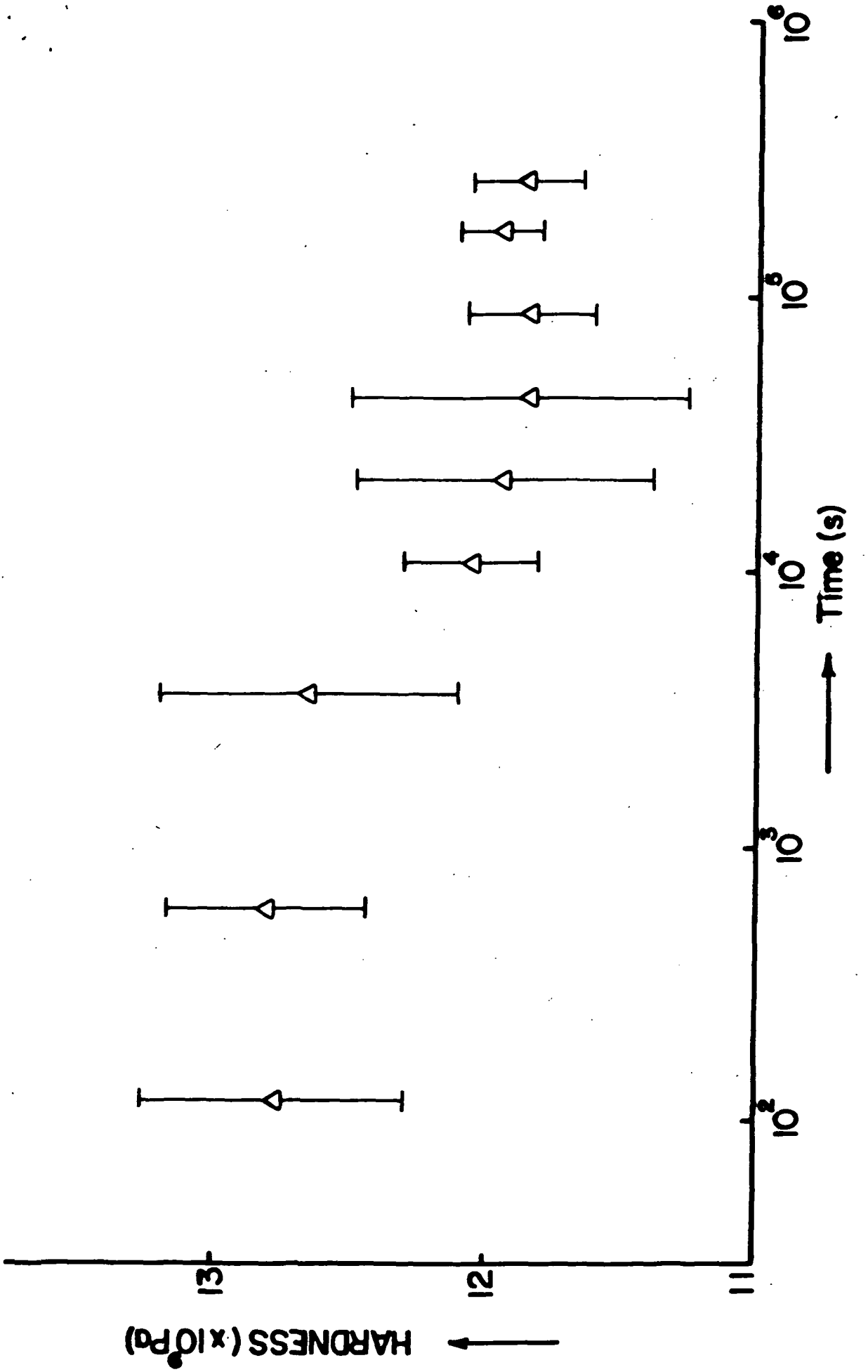

Figure 27 Variation of Hardness versus immersion time in a fluid. In this case the fluid was 100ppm $CaCl_2$ and the indentation load was 0.49N.

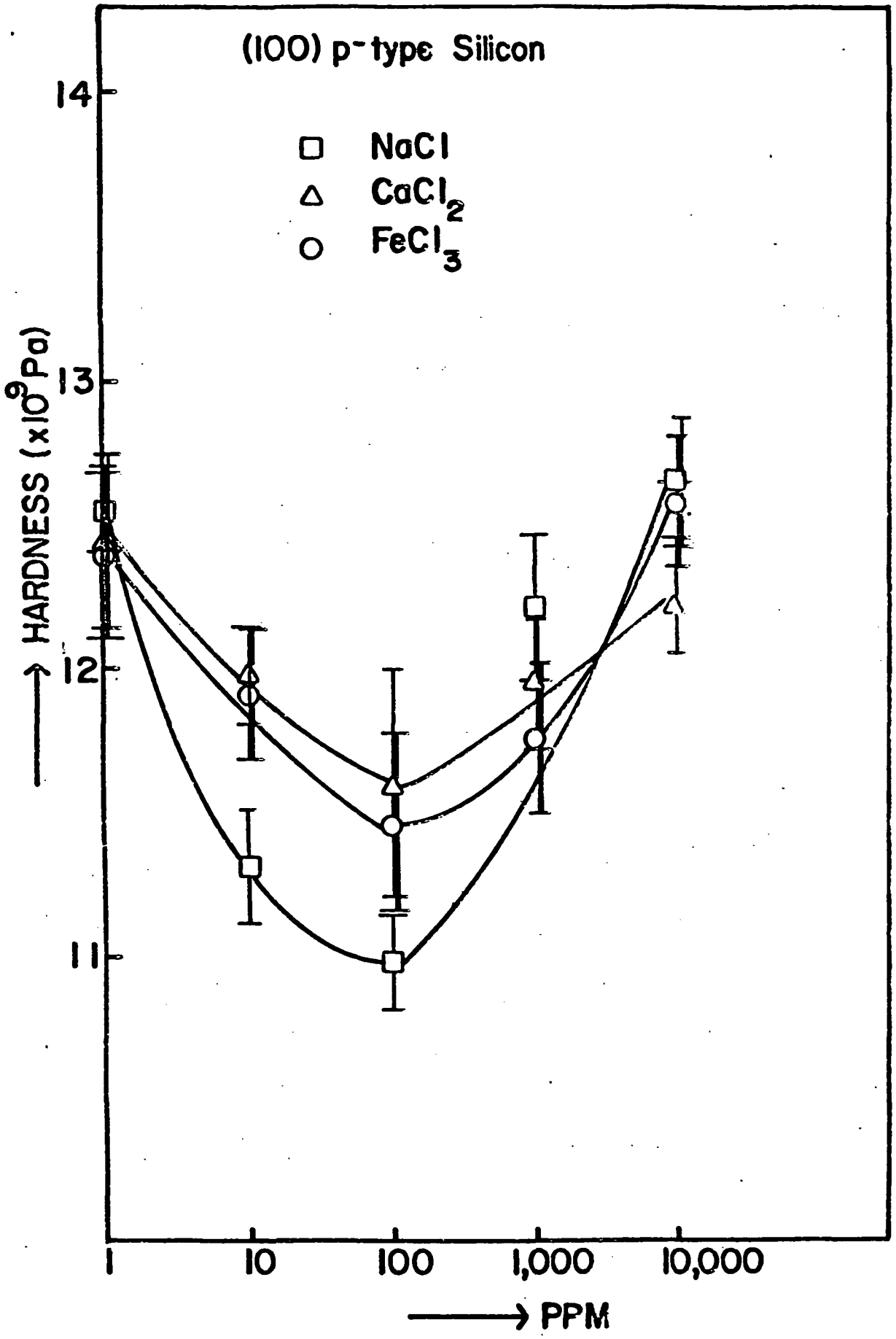

Figure 28 Microhardness (x10^9 Pa) versus salt concentration (ppm) for (100) p-type silicon indented in NaCl, $CaCl_2$ and $FeCl_3$.

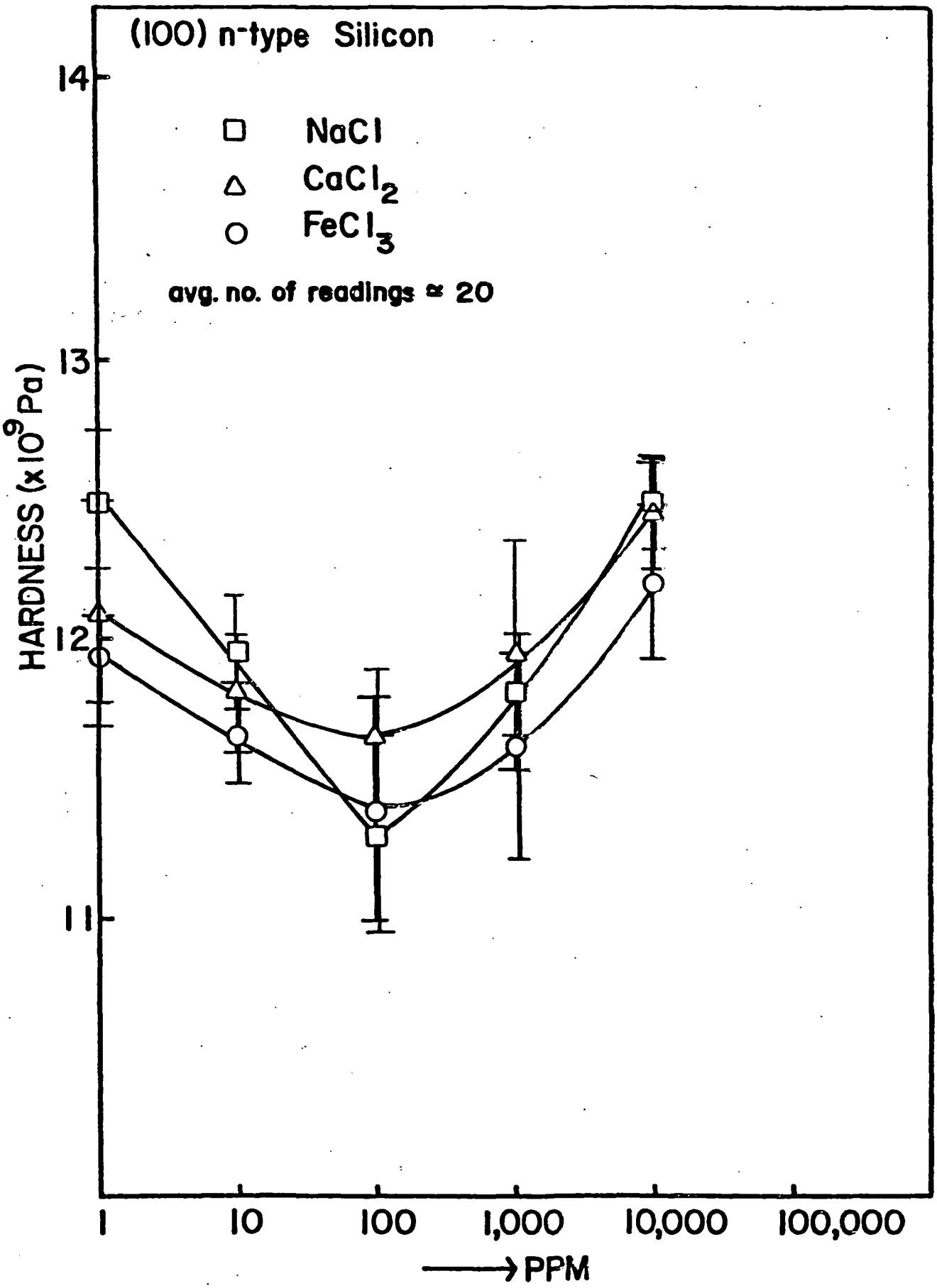

Figure 29 Microhardness ($x10^9$ Pa) versus salt concentration (ppm) for (100) n-type silicon indented in NaCl, $CaCl_2$ and $FeCl_3$.

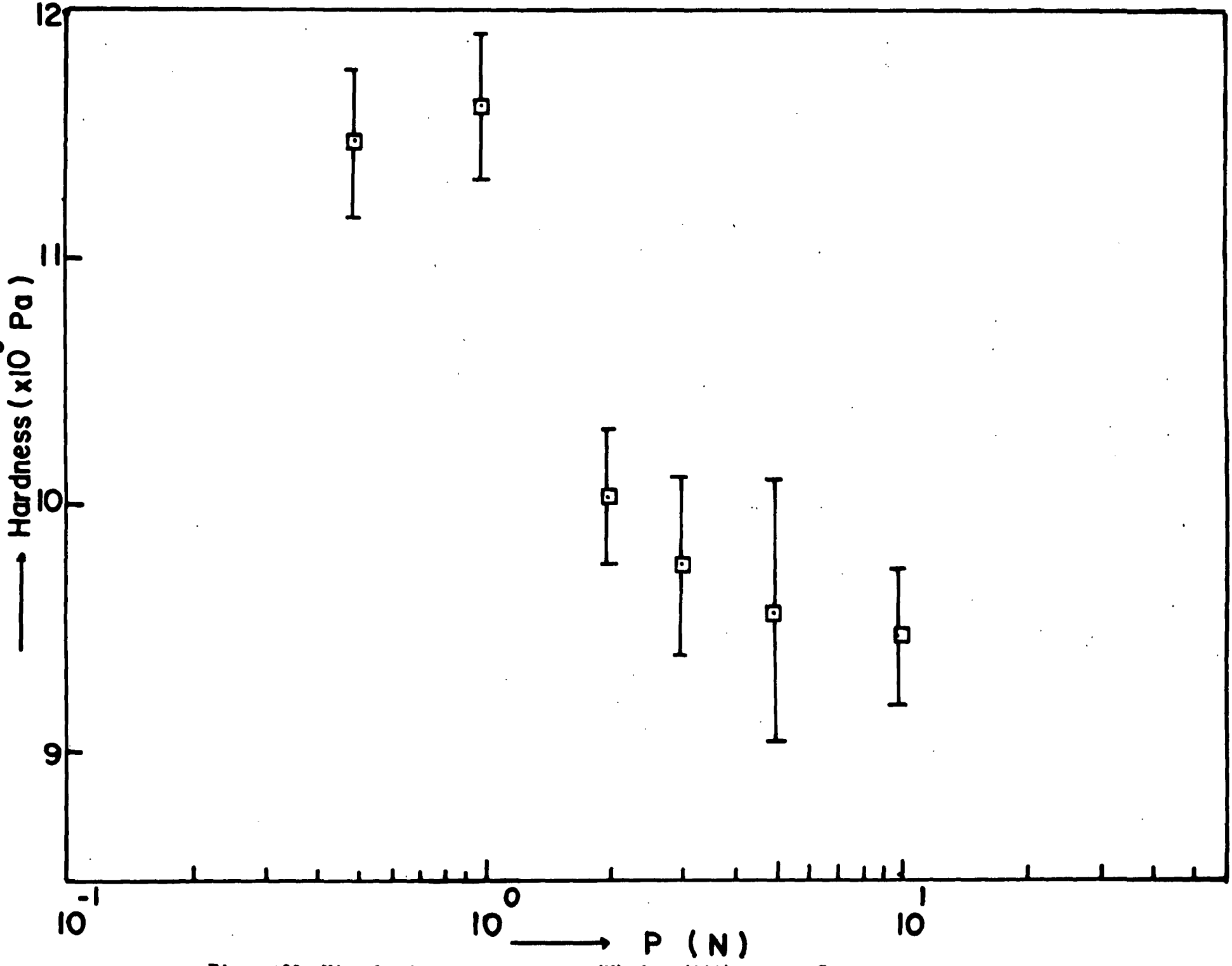

Figure 30 Microhardness versus load (N) for (111) p-type C_z silicon indented in 10^{-3} M/l NaI.

(100) n-type Si

.49N

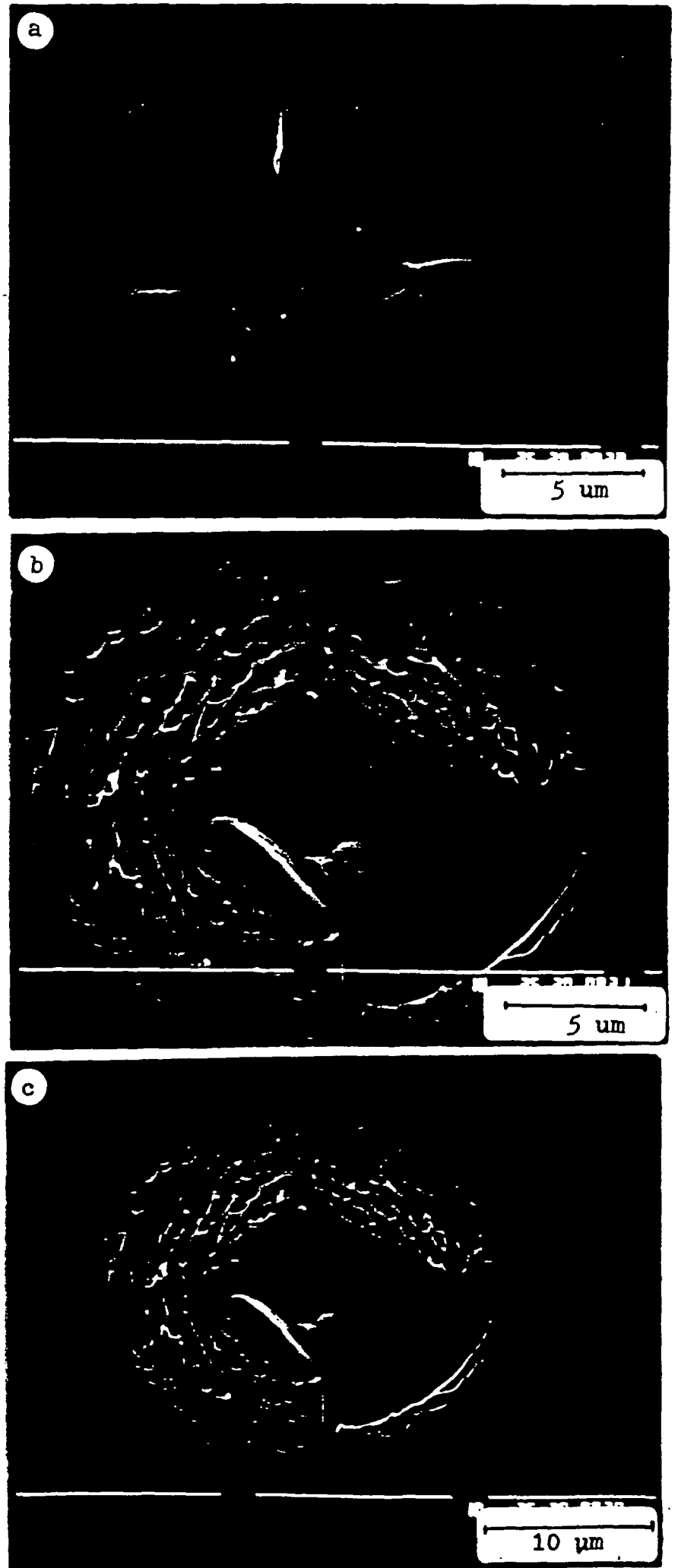

Figure 31 Vickers indentation (P=0.49N) in (100) n-type Cz silicon (a) unetched (b) etched. The indentation was made in de-ionized water containing 1.7×10^{-3} M/ NaCl.

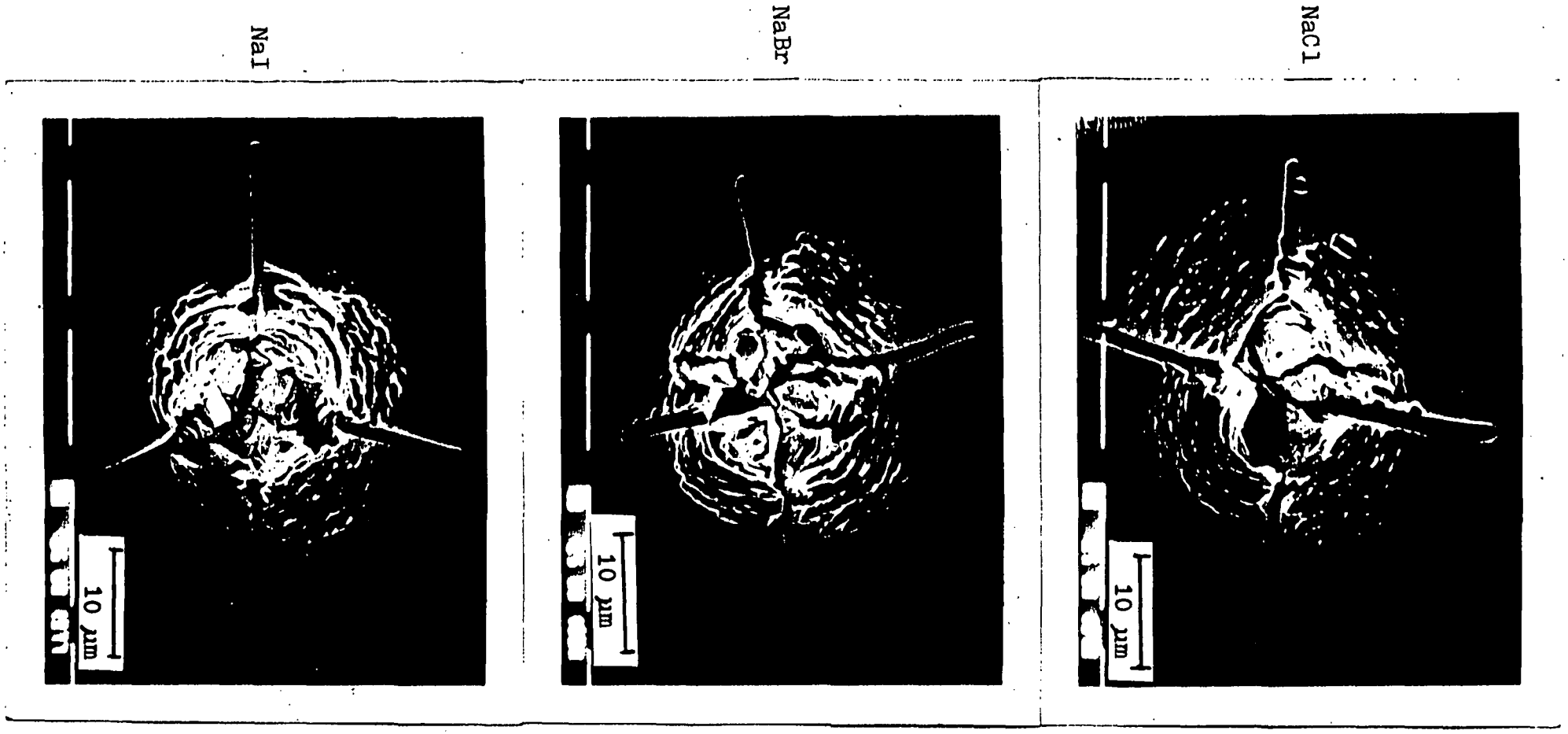

Figure 32 Vickers indentations (P=0.49N) in (111) p-type Cz silicon. The indentations were carried out in (100) ppm NaCl, NaBr and NaI.

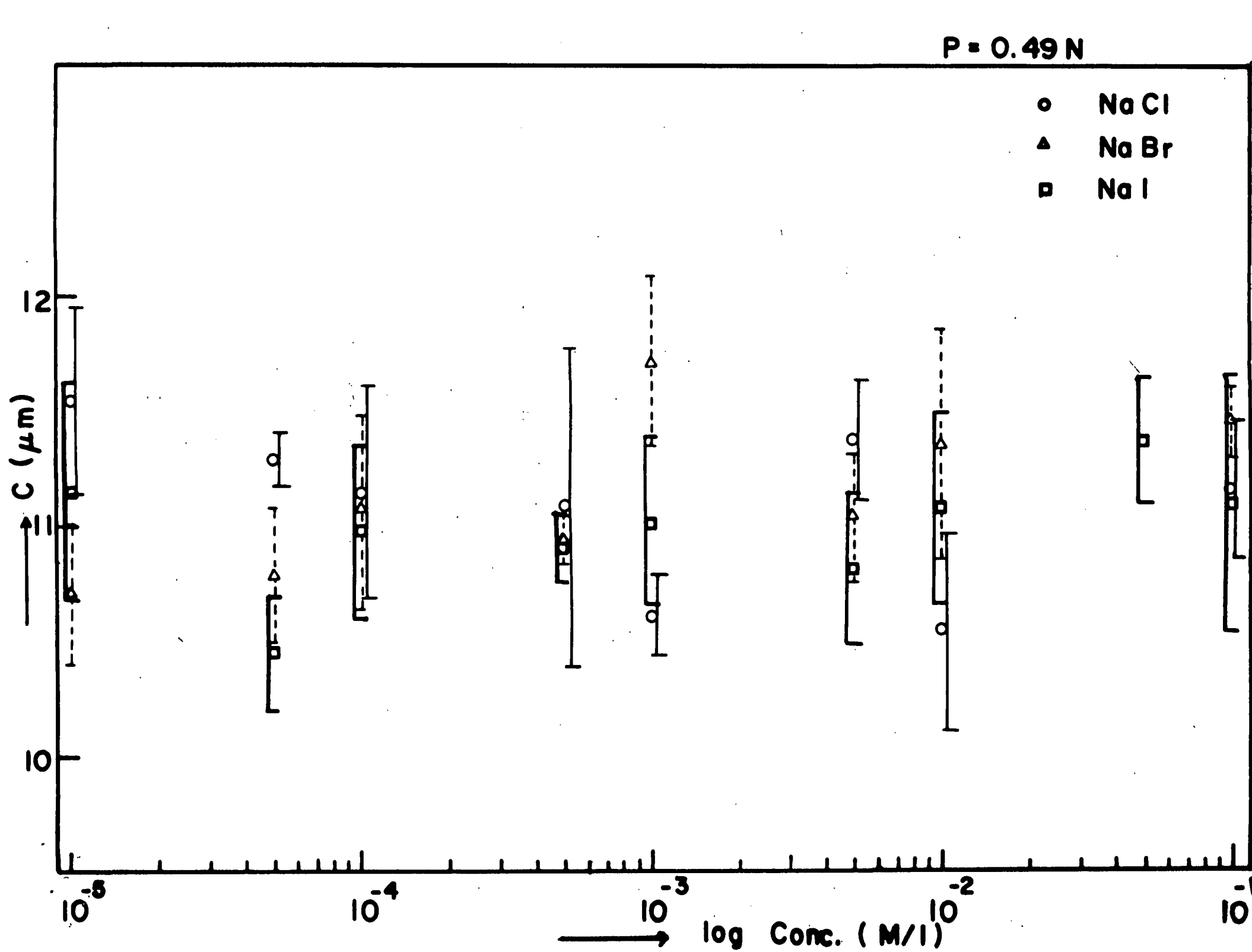

Figure 33 Variation of crack length, c, vs. NaI concentration.

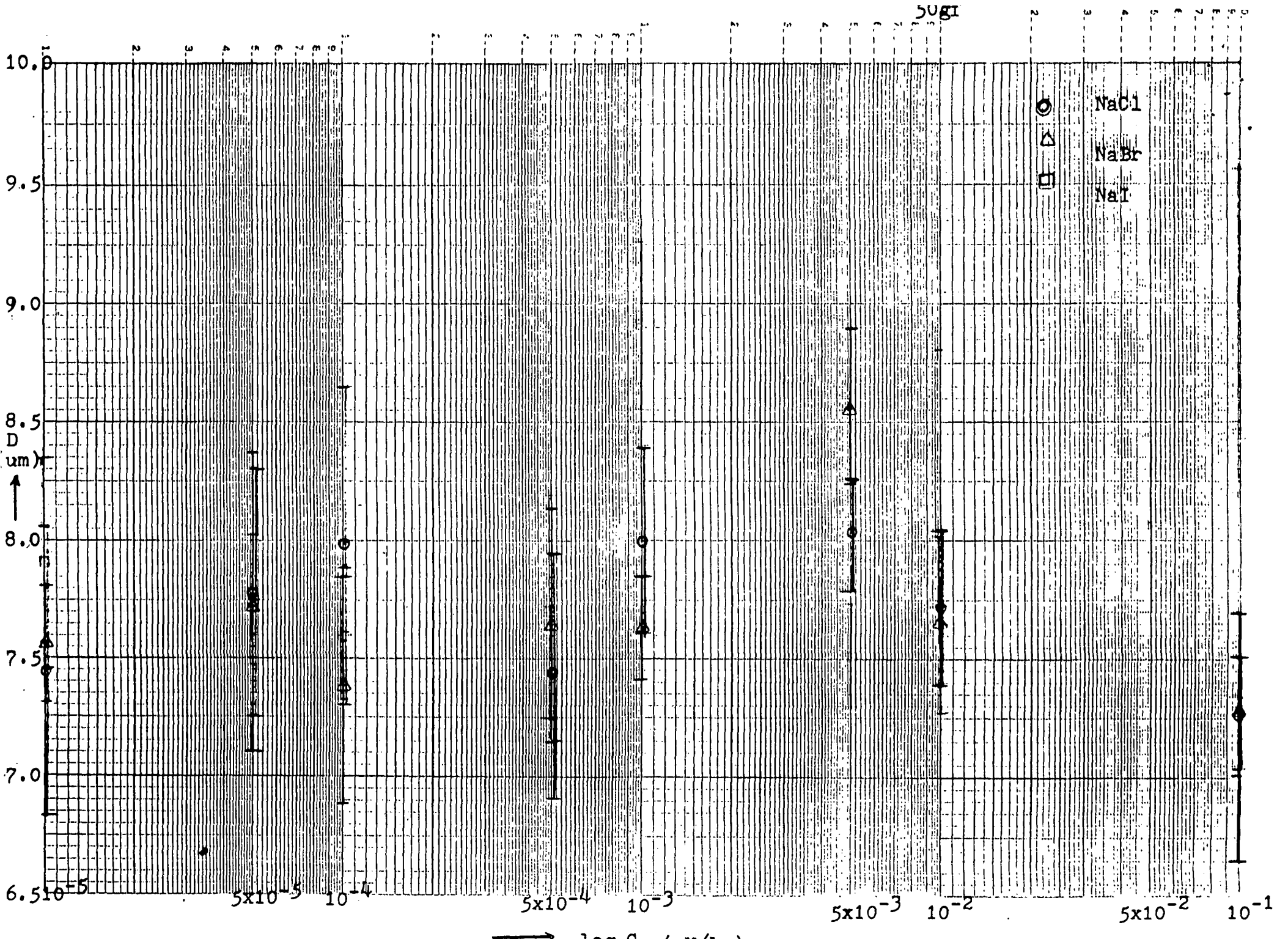

Figure 34 Variation of damage zone D with NaI concentration.

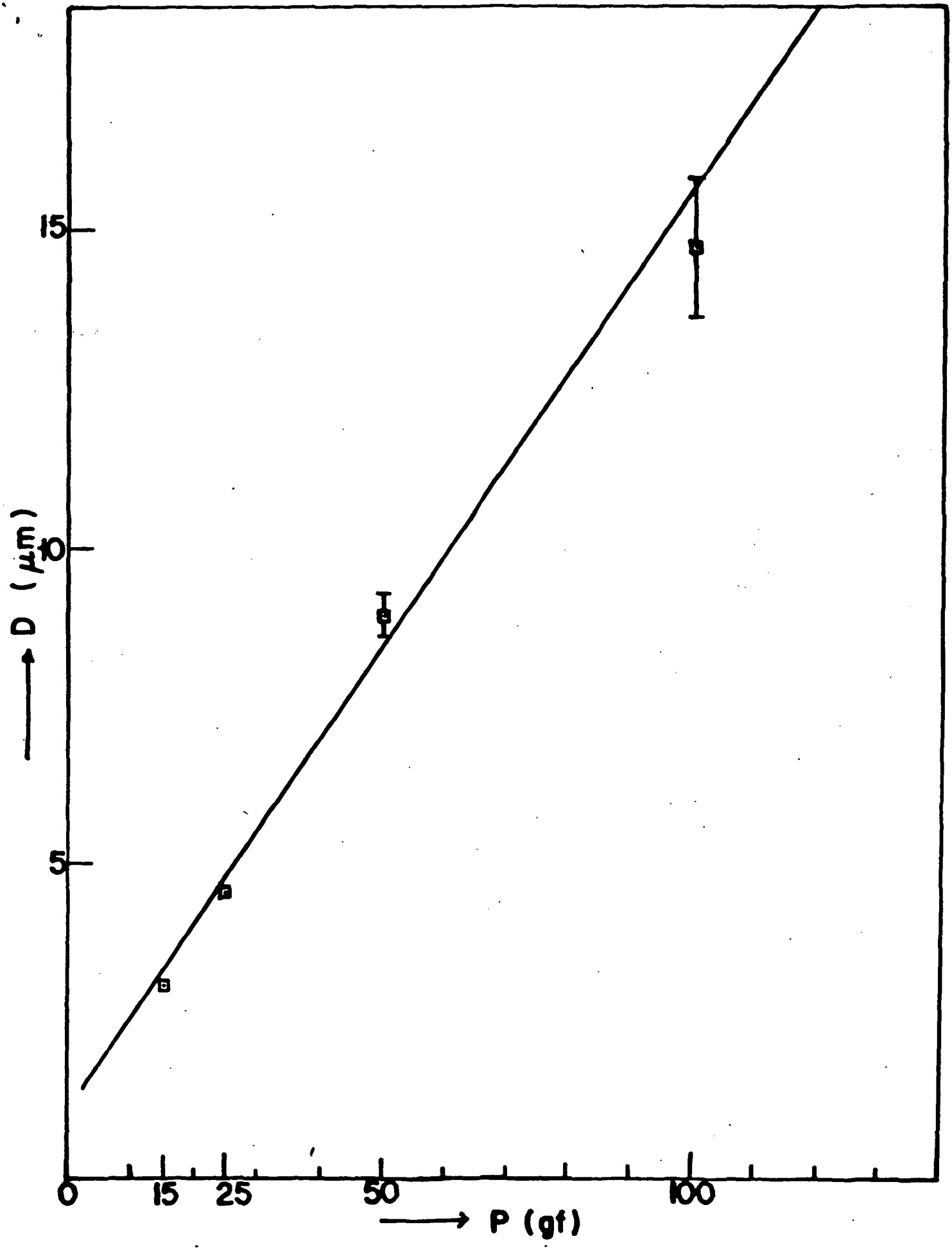

Figure 35 Plot of length of damage zone (D) as a function of indentation load (gf) for (111) p-type silicon indented in 10^{-3} M/l NaI.

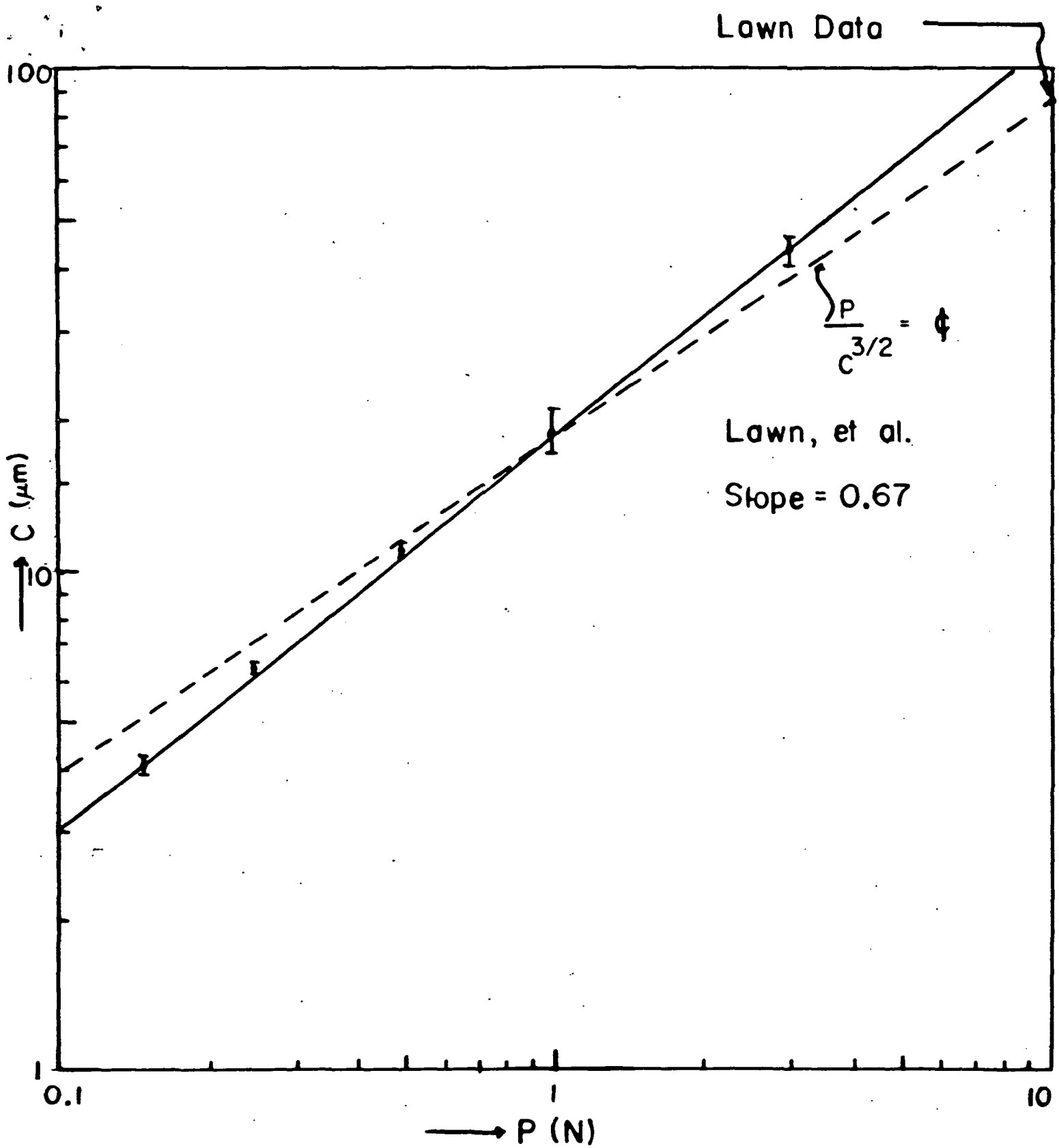

Figure 36 Plot of the crack length, C, versus the load P for (111) p-type silicon indented in 10^{-3} M/l NaI.

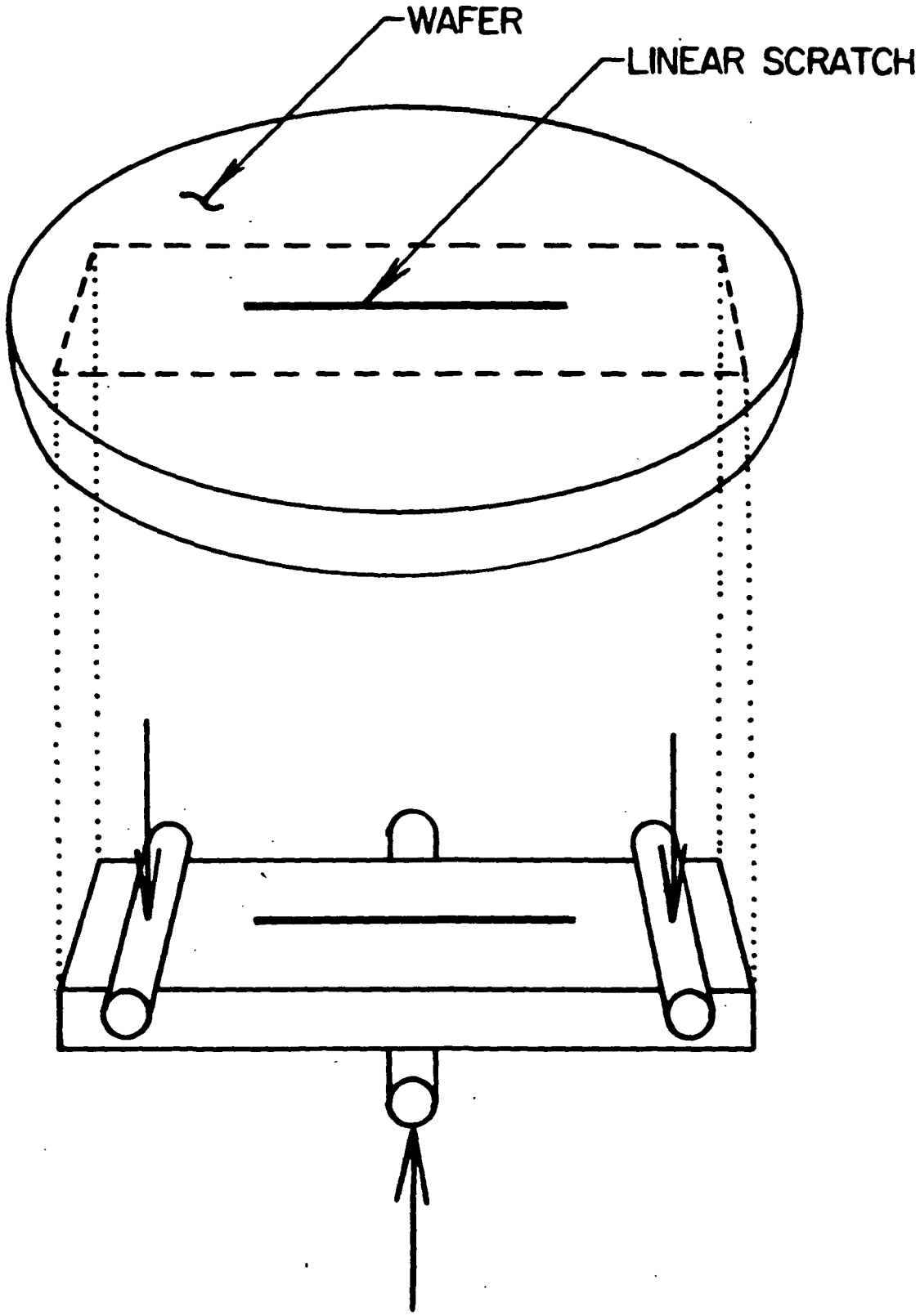

Figure 37 Three-point bend test for determination of fracture strength of silicon. A linear multi-scratch groove is formed in fluids and the fracture strength is obtained.

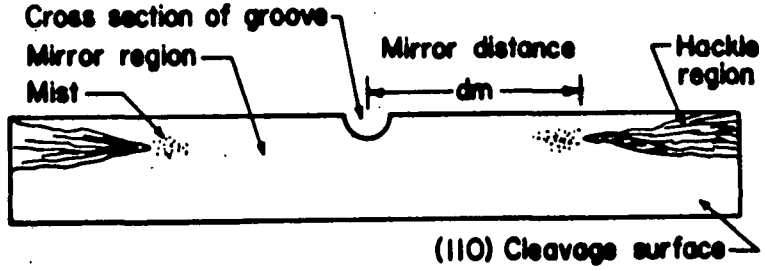

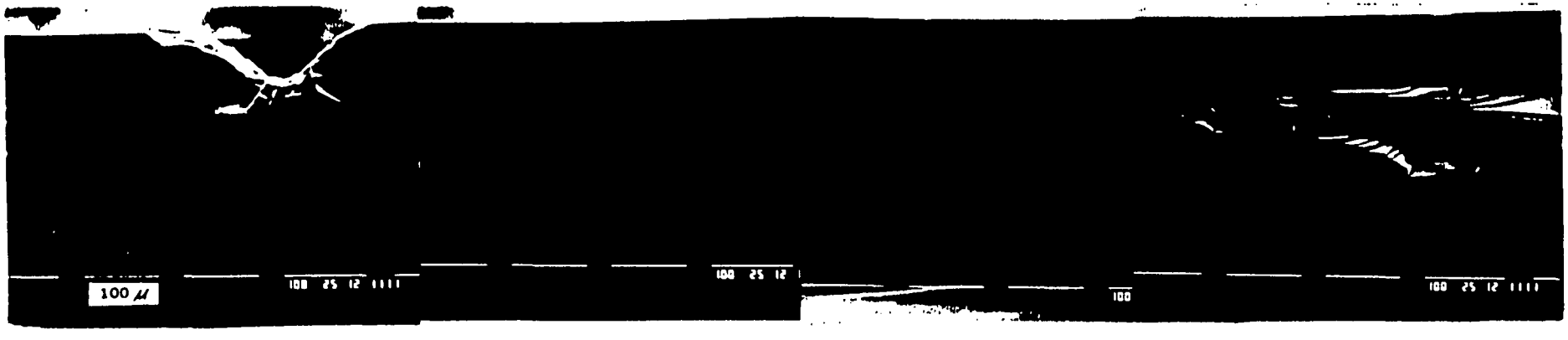

Figure 38 SEM micrograph of the (110) cleavage fracture surface of p-type silicon produced in three-point bending. The linear multiple-scratch groove produced by a 0.54 N dead-loaded pyramid diamond is shown in the cross section. The bend test is conducted in air. Shown in the figure is the groove, mirror and hackle region.

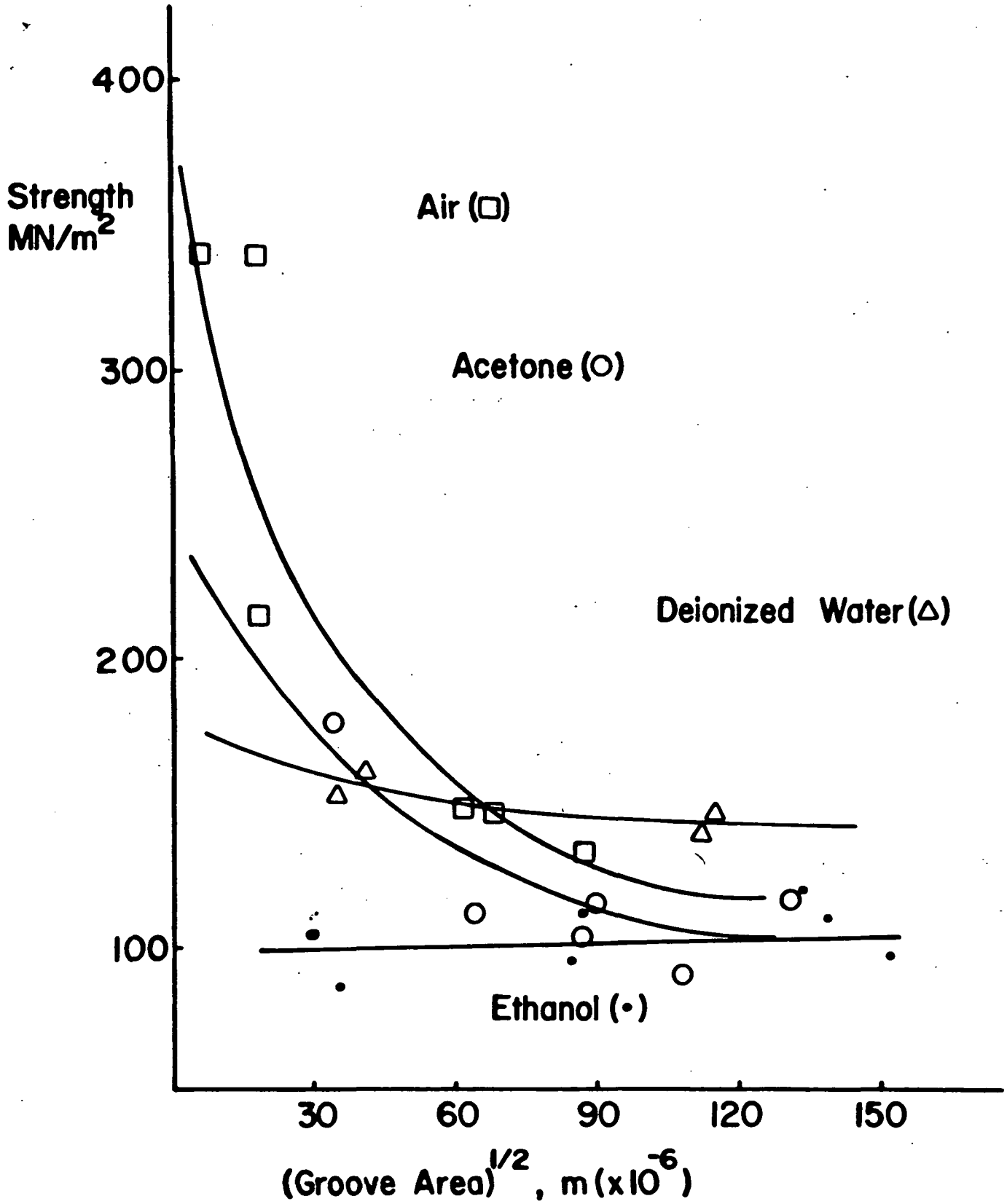

Figure 39 Bending strength (Nm^{-2}) versus groove $area^{1/2}$ (m) of silicon fractured in air. The fluids listed refer to a linear groove that was formed on the (100) surface in the presence of those fluids. The strength is expected to decrease with groove area. The surface mechanical properties are apparently dominated by either the plastic zone or microcracks beneath the groove.

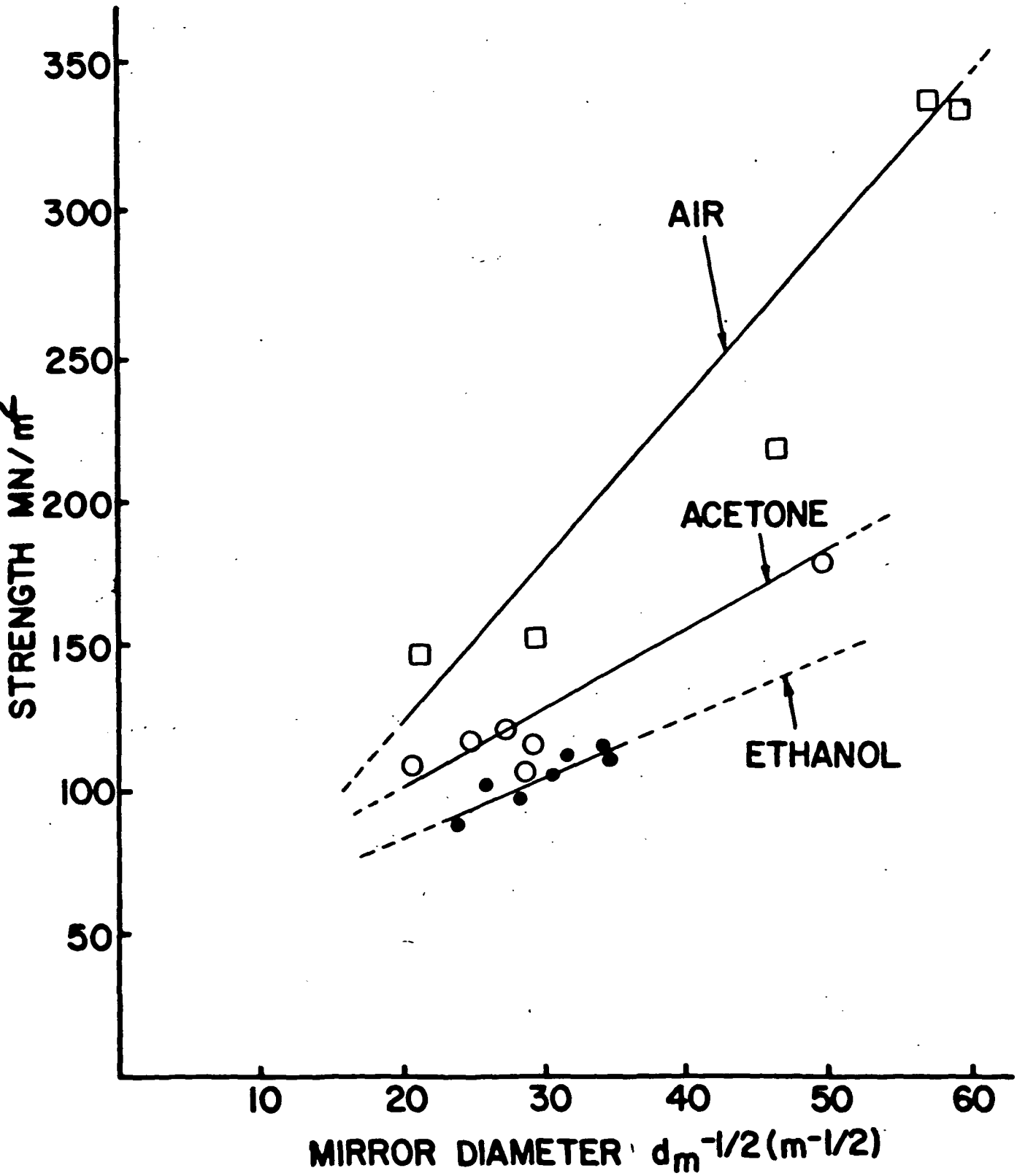

Figure 40 The bending strength versus mirror distance for three-point bend test of (100) p-type silicon. The mirror distance is linear with d_m-1/2. It was expected that all the slopes would be equal if the fluid influenced the depth of the groove and not the surface mechanical properties of silicon. The relation of the σ_f and d_m is $\sigma_f d_m 1/2 = A$ where A is a constant for each fluid.